

UAV-Enabled Wireless-Powered IoT Wireless Sensor Networks

by  
Amin Farajzadeh

Submitted to the Graduate School of Engineering  
and Natural Sciences in partial fulfillment of the requirements  
for the degree of Master of Science

Sabancı University  
Spring 2019

UAV-Enabled Wireless-Powered IoT Wireless Sensor Networks

by Amin Farajzadeh

APPROVED BY

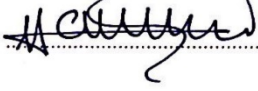
Prof. Dr. Özgür Erçetin  
(Thesis Advisor)



Prof. Dr. Özgür Gürbüz



Prof. Dr. Hakan Ali Çırpan



DATE OF APPROVAL: July 3, 2019

*To my beloved family!*

©Amin Farajzadeh, 2019  
All Rights Reserved

## UAV-Enabled Wireless-Powered IoT Wireless Sensor Networks

Amin Farajzadeh

MSc Thesis, 2019

Thesis Advisor: Prof. Dr. Özgür Erçetin

**Keywords:** *Internet of Things (IoT), Ambient backscattering, Unmanned Aerial Vehicle (UAV), Non-Orthogonal Multiple Access (NOMA), Over-the-Air Computation (AirComp)*

Future massive internet of thing (IoT) networks will enable the vision of smart cities, where it is anticipated that a massive number of sensor devices, in the order of tens of millions devices, ubiquitously deployed to monitor the environment. Main challenges in such a network are how to improve the network lifetime and design an efficient data aggregation process. To improve the lifetime, using low-power passive sensor devices have recently shown great potential. Ambient backscattering is a novel technology which provides low-power long-range wireless communication expanding the network lifetime significantly. On the other hand, in order to collect the sensed data from sensor devices deployed over a wide area, unmanned aerial vehicles (UAVs) has been considered as a promising technology, by leveraging the UAV's high mobility and line-of-sight (LOS) dominated air-ground channels. The UAV can act as data aggregator collecting sensed data from all sensors.

In this thesis, we consider medium-access control (MAC) policies for two sensor data collection scenarios. First, the objective is to collect individual sensor data from the field. The challenge in this case is to determine how a large number of sensors should access the medium so that data aggregation process performed in a fast and reliable fashion. Utilizing conventional orthogonal medium access schemes (e.g., time-division

---

multiple access (TDMA) and frequency-division multiple access (FDMA)), is highly energy consuming and spectrally inefficient. Hence, we employ non-orthogonal multiple access (NOMA) which is envisaged as an essential enabling technology for 5G wireless networks especially for uncoordinated transmissions. In Chapter 2, we develop a framework where the UAV is used as a replacement to conventional terrestrial data collectors in order to increase the efficiency of collecting data from a field of passive backscatter sensors, and simultaneously it acts as a mobile RF carrier emitter to activate backscatter sensors. In the MAC layer, we employ uplink power-domain NOMA scheme to effectively serve a large number of passive backscatter sensors. Our objective is to optimize the path, altitude, and beamwidth of the UAV such that the network throughput is maximized. In Chapter 3, we consider the scenario where there are a separate data collector and RF carrier emitter such that the former is a gateway on the ground and the latter is a single UAV hovering over the field of backscatter sensors. Secondly, we consider a case where only a function of sensed data is of interest rather than individual sensor values. A new challenge arises where the problem is to design a communication policy to improve the accuracy of the estimated function. Recently, over-the-air computation (AirComp) has emerged to be a promising solution to enable merging computation and communication by utilizing the superposition property of wireless channels, when a function of measurements are desired rather than individual in massive IoT sensor networks. One of the key challenges in AirComp is to compensate the effects of channel. Motivated by this, in Chapter 4, we propose a UAV assisted communication framework to tackle this problem by a simple to implement sampling-then-mapping mechanism.

# Acknowledgments

Foremost, I would like to express my sincere gratitude to my advisor Prof. Özgür Erçetin for the continuous support of my research and MSc study, for his patience, motivation, enthusiasm, and immense knowledge. His guidance helped me in all the time of research and writing of this thesis. I have learned a lot from him due to his professional day-to-day supervisory policy and I am sure that this experience will help me tremendously to succeed in my future PhD studies. One of the dominant things that I have learned from him is that it is always possible to appreciate the big picture and the minute details of a complex problem at the same time. I could not have imagined having a better advisor and mentor for my MSc study.

Besides my advisor, I would like to thank my M.Sc defense committee members Prof. Özgür Gürbüz, and Prof. Hakan Ali Çırpan for taking their valuable time attending my defense, and I also thank them for kindly reading the thesis and putting valuable comments.

I also thank Sabanci University for supporting this research work. This thesis is supported by the European Unions Horizon 2020 Research and Innovation Programme under Marie Skłodowska-Curie grant agreement no. 690893.

Last but not the least, I would like to thank my family, for giving birth to me at the first place and supporting me throughout my life.

# Contents

<b>Abstract</b>	<b>v</b>
<b>Contents</b>	<b>vii</b>
<b>List of Figures</b>	<b>x</b>
<b>1 Fundamentals</b>	<b>1</b>
1.1 Overview	1
1.1.1 UAV-Assisted Data Collection	1
1.1.2 Over-the-Air Modulation (Ambient Backscattering)	2
1.1.2.1 Overview	2
1.1.2.2 Long-Range LoRa Backscatter Communications	4
1.1.3 Non-orthogonal Multiple Access (NOMA) Protocol	5
1.1.4 Over-the-Air Computation (AirComp)	6
1.2 Background	7
1.3 Motivation and Contribution	9
1.4 Thesis Outline	10
<b>2 Data Collection in UAV-Assisted NOMA Backscatter Networks</b>	<b>11</b>
2.1 System Model	11
2.1.1 Channel Model	12
2.1.2 Ambient Backscattering	13
2.1.3 Power-Domain NOMA Protocol	14
2.1.4 UAV Mobility Model	16
2.2 Problem Formulation	16
2.2.1 Optimization Problem	20
2.3 Simulation Results	21
<b>3 Data Collection in Hybrid Terrestrial and Aerial NOMA Backscatter Networks</b>	<b>26</b>
3.1 System Model	26
3.1.1 Channel Model	27
3.2 Problem Formulation	28
3.2.1 NOMA Protocol	28
3.2.2 Dynamic-ordered Channel Power Gains	29
3.2.3 Fixed-order Channel Power Gains	33
3.2.4 Optimization Problem	34
3.3 Numerical Results	35

---

<b>4</b>	<b>Data Collection via Over-the-Air Computation in Backscatter Networks</b>	<b>40</b>
4.1	System Model . . . . .	40
4.1.1	Overall Network Model . . . . .	40
4.1.2	Over-the-air functional computation . . . . .	42
4.1.3	Sampling Phase . . . . .	43
4.1.4	Mapping Phase . . . . .	43
4.2	Problem Formulation . . . . .	44
4.2.1	Solution of Optimization Problem . . . . .	45
4.2.2	Heuristic Approach . . . . .	46
4.3	Simulation Results . . . . .	47
<b>5</b>	<b>Summary</b>	<b>50</b>
<b>6</b>	<b>Conclusions and Future Works</b>	<b>52</b>
	<b>Bibliography</b>	<b>53</b>

# List of Figures

1.1	Types of Backscatter Systems [7]. . . . .	3
1.2	Uplink NOMA [14]. . . . .	6
1.3	Downlink NOMA [14]. . . . .	6
2.1	Network model: Target area with hexagonal sub-regions. . . . .	12
2.2	Backscattering setup in one sub-region when the UAV is at an altitude $H$ with an effective illumination angle or beamwidth $\theta$ , serving BNs simultaneously. . . . .	13
2.3	Throughput performance with respect to UAV altitude $H$ , for two different ways of selecting the selection of reflection coefficients $\zeta$ and for three different SINR thresholds $\gamma$ ( $\theta = 60^\circ$ , $\rho = 1$ BNs/m <sup>2</sup> ). . . . .	22
2.4	Throughput performance with respect to the beamwidth $\theta$ and altitude $H$ ( $\gamma = -11.5$ dB, $\rho = 1$ BNs/m <sup>2</sup> ). . . . .	22
2.5	Throughput performance with respect to UAV altitude $H$ , for three different density of BNs $\rho$ on the target area ( $\gamma = -10.5$ dB, $\theta = 60^\circ$ ). . . . .	23
2.6	Throughput performance with respect to the number BNs at each sub-region $N_l$ ( $\theta = 60^\circ$ , $\rho = 1$ BNs/m <sup>2</sup> ). . . . .	24
2.7	Outage performance of three strong BNs $\theta$ with respect to the number BNs at each sub-region $N_l$ ( $\gamma = -10$ dB, $\theta = 60^\circ$ , $\rho = 1$ BNs/m <sup>2</sup> ). . . . .	24
3.1	System Model. . . . .	27
3.2	Throughput Performance considering fixed-ordered decoding scheme with respect to the UAV altitude $H$ . . . . .	36
3.3	Throughput performance considering dynamic-ordered decoding scheme with respect to the UAV altitude $H$ ( $\gamma = 0$ dB). . . . .	36
3.4	Throughput performance considering fixed-ordered decoding scheme respect to the UAV altitude $H$ and beamwidth $\theta$ . ( $\gamma = -7$ dB). . . . .	37
3.5	Throughput performance considering dynamic-ordered decoding scheme respect to the UAV altitude $H$ and beamwidth $\theta$ ( $\gamma = 0$ dB). . . . .	37
3.6	Outage performance of three most strong BNs considering fixed-ordered decoding scheme, with respect to the number BNs $N$ ( $\gamma = -7$ dB). . . . .	38
4.1	Network Model. . . . .	41
4.2	MSE performance vs. the number of samples $K$ ( $N = 50$ , $g_0 = 0.0275$ , $H = 4$ m, $R_{cov} = 4$ m, $P = 30$ dBm). . . . .	48
4.3	MSE performance vs. the number of sensors $N$ ( $K = 5$ , $g_0 = 0.0275$ , $H = 4$ m, $R_{cov} = 4$ m, $P = 30$ dBm). . . . .	48
4.4	MSE performance vs. the number of samples $K$ ( $N = 50$ , $g_0 = 27.5037$ , $H = 75$ m, $R_{cov} = 50$ m, $P = 20$ dBm). . . . .	49

---

4.5	MSE performance vs. the number of sensors $N$ ( $K = 5$ , $g_0 = 27.5037$ , $H = 75$ m, $R_{cov} = 50$ m, $P = 20$ dBm). . . . .	49
-----	---	----

# Chapter 1

## Fundamentals

### 1.1 Overview

Machine type communication (MTC) is one of the enabling technologies of 5G networks. The transmission in MTC network is uplink-dominant and usually requires low data rates. The forecasted huge surge in MTC devices induced the nuisance of massive access at the base station (BS). According to the literature, up to 20 billion IoT devices will be in connected through machine-to-machine (M2M) by the end of 2020. The 5G enabled IoT will connect a large number of IoT devices and make contributions to meet market demand for wireless services. The new requirements of applications in the future IoT and the evolving of 5G wireless technology are two significant trends driving the 5G enabled IoT. Hence, envisioning the future internet of thing (IoT) networks where an enormous number of sensors ubiquitously deployed, will require novel techniques to aggregate the sensed data quickly.

#### 1.1.1 UAV-Assisted Data Collection

Unmanned aerial vehicles (UAVs), also commonly known as drones, have gained wide popularity in the recent years for a variety of applications, such as cargo delivery and aerial imaging [1]. Extensive research efforts from the academia have also been devoted to employing UAVs as different types of wireless communication platforms, such as aerial mobile base stations (BSs), and mobile relays. In particular, employing UAVs as aerial base stations is envisioned as a promising solution to improve the performance of the terrestrial wireless networks [2]. Similarly, there has been a growing research interest in using UAVs for data collection and dissemination in wireless networks, in

order to provide a faster and reliable data collection, longer network lifetime, and real-time data transmission [3], [4]. UAVs have great potential to be employed in long-range backscatter networks to both support more devices and increase the network efficiency and reliability. Consequently, optimizing the 3-D location of the data collecting UAV is very critical in order to provide reliable communication for backscatter devices which operate in the presence of very low power radio frequency (RF) signals.

## 1.1.2 Over-the-Air Modulation (Ambient Backscattering)

### 1.1.2.1 Overview

Ambient backscatter communication technology is a promising candidate for self-sustainable wireless communication systems in which there is no external power supply [5]. By utilizing the existing radio frequency (RF) signal, ambient backscattering technology can support low-power sensor-type devices in the internet of things (IoT) paradigm [6]. In order to support a long-range backscatter communication link the following are needed:

- A backscatter transmitter (tag),
- A backscatter receiver (reader, data collector),
- One (or multiple) carrier emitter (RF energy source).

It should be noted that the emitter may be collocated with the receiver [7]. This novel technology allows to leverage the existing receiver for generating the carrier signal. The state-of-the-art backscatter technology involves the design of a novel backscatter tag that modulates the carrier signal providing long-distance communication while consuming only Ws of power. For instance, the architectures proposed in [8] and [5] promise a long-range backscatter communication. Specifically, [9] achieves a range beyond 3.4 km when operating in the 868 MHz band, and 225 m when operating in the 2.4 GHz band which is a significant improvement over the contemporary in backscatter communications. Hence, through the utilization of designs such as those described in [8] and [9], wide-area communication is enabled by new passive backscatter IoT devices.

Backscatter communications systems can be classified into three main types based on their architectures [7]:

1. *Monostatic Backscatter Communications Systems*: In this type of backscatter systems which can also be considered as Radio-Frequency IDentification (RFID) system, there are two main components: a backscatter transmitter, e.g., an RFID tag,

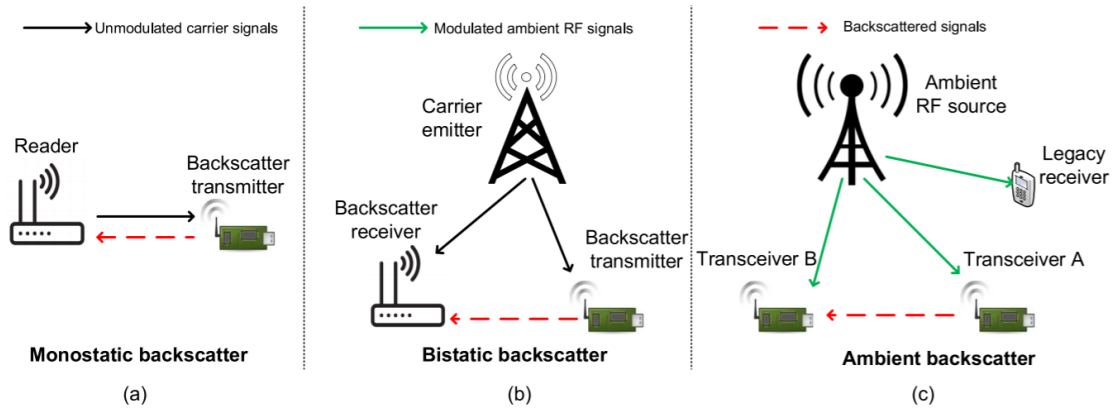


FIGURE 1.1: Types of Backscatter Systems [7].

and a reader as shown in FIGURE 1.1(a). The reader consists of, in the same device, an RF source and a backscatter receiver. The RF source generates RF signals to activate the tag. Then, the backscatter transmitter modulates and reflects the RF signals sent from the RF source to transmit its data to the backscatter receiver. As the RF source and the backscatter receiver are placed on the same device, i.e., the tag reader, the modulated signals may suffer from a round-trip path loss.

2. *Bistatic Backscatter Communications Systems*: Different from Monostatic system, in this type of systems the RF source, i.e., the carrier emitter, and the backscatter receiver are separated as shown in FIGURE 1.1(b). As such, the Bistatic system can avoid the roundtrip path loss as in Monostatic systems. Additionally, its performance can be improved dramatically by placing carrier emitters at optimal locations. Specifically, one centralized backscatter receiver can be located in the field while multiple carrier emitters are well placed around backscatter transmitters. Consequently, the overall field coverage can be expanded. Moreover, the doubly near-far problem can be mitigated as backscatter transmitters can derive unmodulated RF signals sent from nearby carrier emitters to harvest energy and backscatter data. Although carrier emitters are bulky and their deployment is costly, the manufacturing cost for carrier emitters and backscatter receivers of Bistatic is cheaper than that of Monostatic backscatter systems due to the simple design of the components.
3. *Ambient Backscatter Communications Systems*: As illustrated in FIGURE 1.1(c), similar to Bistatic system, carrier emitters in this type of systems are also separated from backscatter receivers. However, different from Bistatic systems, carrier emitters in these systems are available ambient RF sources, e.g., TV towers, cellular base stations, and Wi-Fi access points instead of using dedicated RF sources

as in Bistatic systems. As a result, Ambient backscatter systems have some advantages compared with Bistatic systems. First, because of using already-available RF sources, there is no need to deploy and maintain dedicated RF sources, thereby reducing the cost and power consumption. Second, by utilizing existing RF signals, there is no need to allocate new frequency spectrum, and the spectrum resource utilization can be improved. However, because of using modulated ambient signals for backscatter communications, there are some disadvantages in Ambient systems compared with Bistatic systems. First, modulated ambient RF signals are unpredictable and dynamic, and act as direct interference to backscatter receivers, which largely limits the performance of an Ambient backscatter system, unlike unmodulated ones of the Bistatic system, which can easily be eliminated before backscattered signal detection. Second, since ambient RF sources are not controllable, e.g., transmission power and locations, the design and deployment of an Ambient backscatter system to achieve optimal performance are often more complicated than those of an Bistatic system [7].

### 1.1.2.2 Long-Range LoRa Backscatter Communications

Nowadays, as wireless applications are dynamically expanding their scale, there is a demand for wide area backscatter communications. Hence, Tella *et al.* [8] introduce a backscatter communication system enabling long-range transmissions, namely LoRa. Specifically, LoRa uses the chirp spread spectrum (CSS) modulation which represents a bit ‘0’ as a continuous chirp that increases linearly with frequency, while a bit ‘1’ is a chirp that is cyclically shifted in time. The CSS modulation has several advantages for long-range communications such as achieving high sensitivity and resilient to fading, Doppler, and interference. However, the CSS modulation requires continuously changing the frequency as a function of time. Thus, the authors propose a hybrid digital analog backscatter design which uses digital components to create a frequency plan for the continuously varying CSS signals and map it to analog components by using a low-power digital-to-analog converter (DAC). Furthermore, the authors introduce a backscatter harmonic cancellation mechanism to reduce the interference and improve the system performance. The key idea of this mechanism is adding voltage levels to approximate the sinusoidal signals and obtain a cleaner frequency spectrum. The experimental results show that LoRa can operate at the distance between the RF source and the backscatter receiver up to 475 meters. Additionally, the authors deploy LoRa in different scenarios, i.e., a 446 m<sup>2</sup> house spread across three floors, a 1210 m<sup>2</sup> office area covering 41 rooms, and a one-acre 4046 m<sup>2</sup> vegetable farm, and demonstrate that LoRa backscatter can achieve reliable coverage.

### 1.1.3 Non-orthogonal Multiple Access (NOMA) Protocol

Recently, non-orthogonal multiple access (NOMA) is envisaged as an essential enabling technology for 5G wireless networks especially for uncoordinated transmissions [10]. NOMA exploits the difference in the channel gain among users for multiplexing. By allowing multiple users to be served in the same resource block (to be decoded using successive interference cancellation (SIC)), NOMA may greatly improve the spectrum efficiency and may outperform traditional orthogonal multiple access schemes in many scenarios [11]. Moreover, it can support massive connectivity, since a large number of users can be served simultaneously [12]. Also Due to the simultaneous transmission nature, a user does not need go through a scheduled time slot to transmit its information, and hence, it experiences lower latency. NOMA can also maintain user-fairness and diverse quality of service by flexible power control between the strong and weak users; particularly, as more power is allocated to a weak user, NOMA offers higher cell-edge throughput and thus enhances the cell-edge user experience. Basically, NOMA can be categorized into two major types:

1. *Power-domain NOMA*: In this type of NOMA, at the transmitter, different signals generated by different devices are directly superimposed on each other after conventional channel coding and modulation. Multiple devices share the same time-frequency resources, and then are decoded at the receivers using SIC. As a result, the spectral efficiency can be improved at the cost of an increased receiver complexity compared to conventional orthogonal multiple access (OMA). Additionally, it is widely recognized based on information theory that non-orthogonal multiplexing using superposition coding at the transmitter and SIC at the receiver not only outperforms classic orthogonal multiplexing, but it is also optimal from the perspective of achieving the capacity region of the downlink broadcast channels [13]. In this thesis, the uplink power-domain NOMA is employed.
2. *Code-domain NOMA*: The concept of code-domain NOMA is inspired by the classic code-division multiple access (CDMA) systems, in which multiple users share the same time-frequency resources, but adopt unique user-specific spreading sequences. However, the key difference compared to CDMA is that the spreading sequences are restricted to sparse sequences or non-orthogonal low cross-correlation sequences in NOMA [13].

As illustrated in FIGURE 1.2, in uplink NOMA, the idea is that the nodes with strong channel gains (channel between node and the base station (BS)) transmit their data with high power level; hence, the node with the strongest channel gain has that

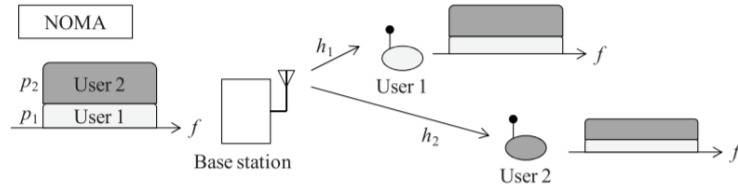


FIGURE 1.2: Uplink NOMA [14].

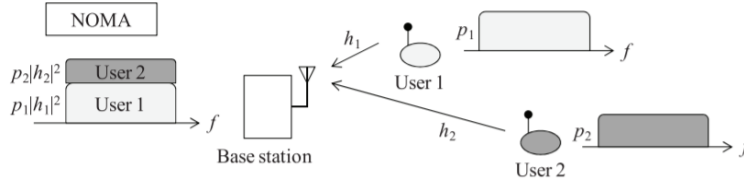


FIGURE 1.3: Downlink NOMA [14].

highest transmission power, and the weakest node has the lowest power. On the other side, in downlink NOMA, the transmitted signal from the BS to the node with strongest channel gain has the lowest power while to the node weakest channel gain, it has the highest power, as illustrated in FIGURE 1.3.

#### 1.1.4 Over-the-Air Computation (AirComp)

The future IoT network is anticipated to connect an enormous number of sensors (e.g., billions). For instance, the future cellular 5G systems is expected to connect more than 1 trillion devices [15]. As a result, this makes the conventional data aggregation policy of aggregate-then-compute an impractical multiple access scheme for networks with massive number of devices since it has high delay performance [16]. To overcome this challenge, a promising technique called over-the-air function computation (AirComp) was proposed which utilizes the superposition property of wireless channel to compute functions via concurrent transmission over a multiple access channel (MAC) [17]. In fact, AirComp is a wireless system that allows a collection of sensors to transmit their data concurrently such that the receiver receives over the medium a nomographic function of the sensors' data. The well-known nomographic functions are listed in TABLE 1.1. The idea of AirComp can be tracked back to the pioneer work studying functional computation in sensor networks [18]. In [18], structured codes (e.g., lattice codes) are designed for reliably computing at an access point (AP) a function of distributed sensing values transmitted over a MAC. The significance of the work lies in its counter-intuitive finding that “interference” can be harnessed to help computing. Subsequently, it was proved that the simple analog transmission without coding, where transmitted signals are scaled versions of sensing values, can achieve the minimum functional distortion

TABLE 1.1: Nomographic Functions

Name	Function
Arithmetic Mean	$f = \frac{1}{K} \sum_{k=1}^K d_k$
Weighted Mean	$f = \sum_{k=1}^K w_k d_k$
Geometric MEan	$f = \left( \prod_{k=1}^K d_k \right)^{\frac{1}{K}}$
Polynomial	$f = \sum_{k=1}^K w_k d_k^{v_k}$
Euclidean Norm	$f = \sqrt{\sum_{k=1}^K d_k^2}$

achievable by any scheme [19]. On the other hand, coding can be still useful for other settings such as sensing correlated Gaussian sources [20]. The satisfactory performance (with optimality in certain cases) of simple analog AirComp have led to an active area focusing on designing and implementing techniques for receiving a desired function of concurrent signals, namely a targeted coherent combination of the signal waveforms [17],[21].

The implementation of AirComp faces several practical issues. One is the synchronization of all active sensors required for coherent combining at the AP. To cope with synchronization errors, a solution, called AirShare, was developed in [22] for synchronizing sensors by broadcasting a reference-clock signal and its effectiveness was demonstrated using a prototype. AirShare is a simple low-overhead system that synchronizes nodes by transmitting the reference clock over the air, providing a tool for generic distributed physical layer (PHY) protocols.

To put it in nutshell, the underlying basics and major assumptions in AirComp can be summarized as follows:

- AirComp is targeted towards large and dense sensor networks, which incur a high overhead from collecting individual sensor measurements from all the sensors, and can therefore obtain significant benefit from over-the-air aggregation of these measurements.
- Sensors can transmit their data coherently (i.e., synchronized in time and phase). Sensors can do so using recently developed synchronization techniques such as AirShare [22].

## 1.2 Background

In the literature, there are many studies on optimizing the 3-D location of the aerial base stations under various scenarios. For instance, in [23], the authors aim to optimize

the UAV's altitude and antenna beamwidth for throughput maximization in three different communication models without considering the impact of altitude and beamwidth on the flight time. In [24], a particle swarm optimization algorithm is proposed to find an efficient 3D placement of a UAV that minimizes the total transmit power required to cover the indoor users without discussing the outage performance and its dependency on the UAV's altitude. The impact of the altitude on the coverage range of UAVs was studied in [25]. In [26], an optimum placement of multiple UAVs for maximum number of covered users is investigated. In [27], the authors aimed to find the optimal altitude which maximizes the reliability and coverage range. They consider the dependence of the path-loss exponent and multi-path fading on the height and angle of the UAV; however, similar to the previous works, they do not consider the impact of UAV's altitude on its flight time. Another drawback of the previous approaches is the lack of discussion on the control of ground networks with limited or no energy supplies. In this work, we consider passive devices which have no power supply, and investigate how their passive nature can impact the network performance.

In addition, in [3] and [4], the authors consider a scenario where an UAV collects data from a set of sensors. In particular, in [3], they jointly optimize the scheduling policy and UAV's trajectory to minimize the maximum energy consumption of all sensors, while ensuring that the required amount of data is collected reliably from each node. In [4], the authors investigate the flight time minimization problem for completing the data collection mission in a one-dimensional sensor network. The objective is to minimize the UAV's total flight time from a starting point to a destination while allowing each sensor to successfully upload a certain amount of data using a given amount of energy. However, in these works, all the ground nodes are active devices which access the channel based on the conventional medium access control (MAC) protocols.

In [28], the authors investigate the applicability of NOMA for UAV-assisted communication systems. It is shown that the performance of NOMA scheme is far better than the orthogonal multiple access scheme under a number of different scenarios. Furthermore, in [29], a NOMA-based terrestrial backscatter network is studied where the results suggest that NOMA has a good potential for being employed in backscatter communications.

On the other hand, when it comes to collect and compute a function sensed data rather than individual sensed data, there few works on the literature which basically employ AirComp concept to achieve this goal. For instance, in [30–32], the authors aim at developing multiple-input-multiple output (MIMO) AirComp such that the objective is to find the optimal beamforming design for compensating the nonuniform fading. In order to compensate the non-uniform fading of different sensors, they propose a novel uniform-forcing transceiver design for over-the-air function computation, and a min-max optimization problem is formulated to minimize the accuracy of the computation which

is measured by mean squared error. Moreover, considering analog AirComp, in [33], an analog function computation scheme was proposed which was robust against synchronization errors utilizing random sequences. Power control at sensors was also optimized in [21, 34], the computation rate (defined as the number of functional values computed per time slot) analyzed in [34], and the effect of channel estimation error characterized in [35]. More recently, in [36], a multi-antenna UAV-enabled AirComp is studied where UAV acts both as data collector and wireless power transmitter. The objective in this work was to jointly design an optimal power allocation, energy beamforming and AirComp equalization to minimize the MSE. However, the mobility of the UAV was not taken into account in improving the MSE performance.

### 1.3 Motivation and Contribution

In future massive internet of thing (IoT) networks, e.g., smart cities, it is anticipated that an enormous number of sensor devices, e.g. tens of millions, ubiquitously will be deployed to measure various parameters. The main challenges in such a networks are how to improve the network lifetime and design an efficient data aggregation process. To improve the lifetime, using low-power passive sensor devices have recently shown great potential. Ambient backscattering is a novel technology which provides low-power long-range wireless communication expanding the network lifetime significantly. On the other side, in order to collect the sensed data from sensor devices in a wide area, most recently UAVs has been considered as a promising technology which expands network coverage and enhances system throughput, by leveraging the UAV's high mobility and line-of-sight (LOS) dominated air-ground channels. Depending on the application, the data collector (UAV) can whether collect sensed data from all sensors individually or collect a function of sensed data. In each case, several challenges comes up which require novel techniques to employ.

To be more precise, when the objective is to collect individual sensed data from sensors, the main challenge is how efficiently these massive number of sensors should access the medium so that data aggregation process performed in a fast and reliable fashion. Utilizing conventional orthogonal medium access schemes (e.g., time-division multiple access (TDMA) and frequency-division multiple access(FDMA)), will be highly energy consuming and spectrally inefficient. Hence, employing an efficient scheme is critical to serve a large number of sensors. Recently, non-orthogonal multiple access (NOMA) is envisaged as an essential enabling technology for 5G wireless networks especially for uncoordinated transmissions. It has been shown that NOMA may greatly improve the spectrum efficiency and may outperform traditional orthogonal multiple access schemes in many scenarios since a large number of users can be served simultaneously. Motivated

by this, in Chapter 2, we develop a framework where the UAV is used as a replacement to conventional terrestrial data collectors in order to increase the efficiency of collecting data from a field of passive backscatter sensors, and simultaneously it acts as a mobile RF carrier emitter to activate backscatter sensors. In the MAC layer, we employ uplink power-domain NOMA scheme to effectively serve a large number of passive backscatter sensors. Our objective is to optimize the mobility of the UAV such that the network throughput is maximized. Moreover, in Chapter 3, we consider a separate data collector and RF carrier emitter such that the former is a gateway on the ground and the latter is a single UAV hovering over the field of backscatter sensors.

In the second case, where a function of sensed data is desired to be collected and computed, a new challenge comes to the picture and it is that how to design a communication policy to improve the accuracy of the estimated function. Recently, over-the-air computation (AirComp) has emerged to be a promising solution to enable merging computation and communication by utilizing the superposition property of wireless channels, when a function of measurements are desired rather than individual in massive IoT sensor networks. One of the key challenges in AirComp is to compensate the effects of channel. Motivated by this, in Chapter 4, we propose a UAV assisted communication framework to tackle this problem by a simple sampling-then-mapping mechanism.

To put it in a nutshell, our main objective in this thesis, is to optimally utilize the mobility of the UAV as its main advantage, in order to tackle the aforementioned challenges in collecting the sensed data from a massive low-power passive devices, and improve the network performance.

## 1.4 Thesis Outline

The rest of the thesis is organized as follows. In Chapter 2, we study the network throughput performance of a UAV-assisted NOMA backscatter network where the UAV acts both as carrier emitter and data collector. In Chapter 3, we describe a NOMA backscatter network model where the carrier emitter and data collector are considered to be separate. We proceed with studying UAV-assisted AirComp backscatter sensor networks in Chapter 4, where the network performance metric is also evaluated. Finally, Chapter 6 concludes this thesis.

## Chapter 2

# Data Collection in UAV-Assisted NOMA Backscatter Networks

### 2.1 System Model

In this chapter, we consider a UAV-assisted NOMA backscatter network where  $N$  BNs are distributed independently and uniformly (i.e., binomial point process) in a area of size  $\mathcal{A}$  m<sup>2</sup> with density  $\rho = \frac{N}{\mathcal{A}}$  BNs/m<sup>2</sup>. As shown in FIGURE 2.1, we assume that there is a single UAV equipped with a directional antenna with adjustable beamwidth  $\theta$ , which acts both as RF carrier emitter and data sink. The UAV hovers over the target area for a fixed duration  $T_f$  while continuously broadcasting a single carrier RF signal with fixed power  $P_u$  to BNs on the ground that utilize the received RF signal to backscatter their data to the UAV, simultaneously, based on power-domain NOMA scheme. We also assume that the target area is sufficiently large such that it can be partitioned into

$$W = \frac{\mathcal{A}}{A_l}, \forall l = 1, \dots, W, \quad (2.1)$$

sub-regions with hexagonal shapes where  $A_l$  is the coverage area of the UAV when it hovers over sub-region  $s_l$  at altitude  $H$  with beamwidth  $\theta$  and radius  $r = H \tan \frac{\theta}{2}$  as illustrated in FIGURE 2.2. Thus, the average number of BNs covered by the UAV at sub-region  $s_l$  is given by

$$\bar{N}_l = \frac{3\sqrt{3}}{2} \rho H^2 \tan^2 \frac{\theta}{2}. \quad (2.2)$$

The number of sub-regions  $W$  implies that the UAV's total flight time,  $T_f$ , is divided into  $W$  sub-slots where each sub-slot has the same duration of  $T$ , i.e.,  $T_f \geq \sum_{l=1}^W T$ .

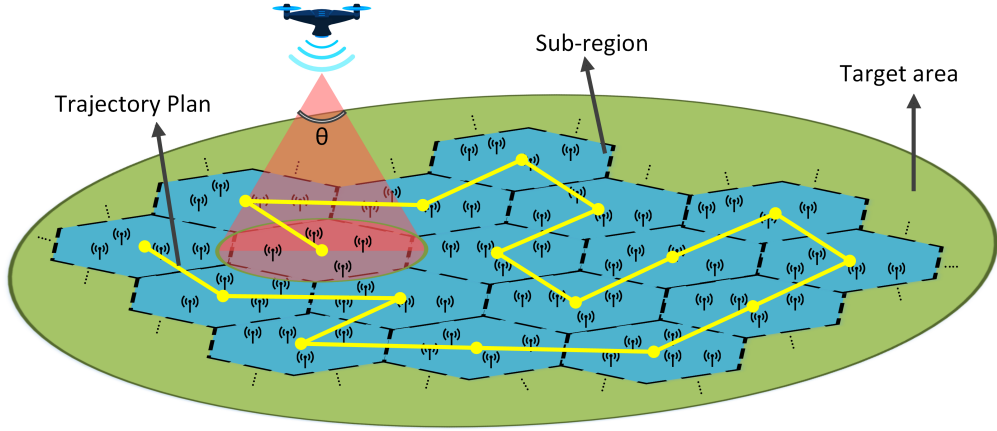


FIGURE 2.1: Network model: Target area with hexagonal sub-regions.

Furthermore, we assume that the UAV's flying speed is sufficiently high, i.e.,

$$T_f(\theta, H) \approx W(\theta, H)T. \quad (2.3)$$

FIGURE 2.1 illustrates the geometry of dividing the target area into sub-regions. The BNs backscatter to the UAV at most only once since each BN switches to sleep mode until the end of UAV's flight time after backscattering its data. For simplicity, we assume that the azimuth and elevation half-power beamwidths of the UAV antenna are equal, which are both denoted as  $\theta$ , with  $\theta \in (0, \frac{\pi}{2})$ . Moreover, the corresponding antenna gain in direction  $(\Theta, \Phi)$  is approximately modeled as

$$G = \begin{cases} \frac{G_0}{(\frac{\theta}{2})^2}, & \text{if } 0 \leq \Theta \leq \theta \text{ and } 0 \leq \Phi \leq \theta, \\ g, & \text{otherwise,} \end{cases} \quad (2.4)$$

where  $G_0 \approx 2.2846$ ,  $\Theta$  and  $\Phi$  denote the azimuth and elevation angles, respectively. Also,  $g$  is the channel gain outside the beamwidth of the antenna and satisfies  $0 < g \leq \frac{G_0}{(\frac{\theta}{2})^2}$ . In this work, for simplify, we consider  $g = 0$ .

### 2.1.1 Channel Model

We consider a path-loss model in which the channel power gain of the link between the UAV and BN  $i$ ,  $i = 1, \dots, N$ , is defined as  $h_{BN_i} d_{BN_i}^{-\alpha}$  where  $h_{BN_i} = 10^{\frac{g_{BN_i}}{10}}$  denotes the shadowing effect following a log-normal distribution. Let  $g_{BN_i}$  be a Normal distributed random variable with variance  $\sigma^2$ , and  $d_{BN_i}^{-\alpha}$  denotes the distance-dependent attenuation in which  $\alpha$  is the path-loss exponent and  $d_{BN_i}$  is the distance between BN  $i$  and the

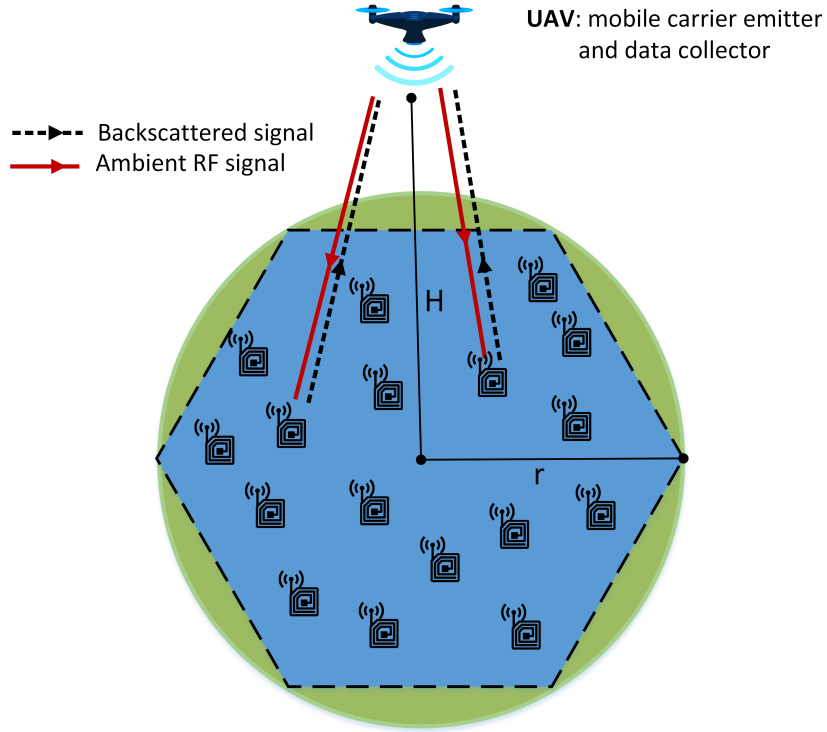


FIGURE 2.2: Backscattering setup in one sub-region when the UAV is at an altitude  $H$  with an effective illumination angle or beamwidth  $\theta$ , serving BNs simultaneously.

UAV. Let  $(x, y, H)$  be the 3-D coordinates of the UAV. Thus, the distances between the UAV and any BN can be calculated as

$$d_{BN_i} = \sqrt{H^2 + (x_{BN_i} - x)^2 + (y_{BN_i} - y)^2}, \quad (2.5)$$

where  $x_{BN_i}$  and  $y_{BN_i}$  are the coordinates of BN  $i$ . In this work, we assume that the UAV knows the exact location of the BNs. In the following, we discuss the ambient backscattering and power domain NOMA scheme which are employed in this work.

### 2.1.2 Ambient Backscattering

Upon receiving RF signal from the UAV, the BNs use a modulation scheme (e.g. FSK) to map their data bits to the received RF signal and then backscatter them to the UAV, simultaneously, for a duration of  $T$  time units. After the transmission, BN switches to the sleep mode and remains at this mode until the end of the UAV's total flight time. The received power at BN  $i$  can be written as

$$P_{BN_i}^{rx} = GP_u h_{BN_i} d_{BN_i}^{-\alpha}. \quad (2.6)$$

The probability density function of this slowly varying received power by the BN  $i$  is given by

$$f_h(v) = \frac{1}{a\sigma v\sqrt{\pi}} \exp -\left(\frac{\ln(v) - am}{\sqrt{2}\sigma}\right)^2, \quad (2.7)$$

where  $a = \frac{\ln 10}{10}$  and  $m = \frac{1}{a} \ln(GP_u d_{BN_i}^{-\alpha})$  is the logarithmic received mean power expressed in decibels (dB), which is related to the path-loss and  $\sigma$  is the (logarithmic) standard deviation of the mean received signal due to the shadowing.

Let  $\zeta_{BN_i}$  be the reflection coefficient of BN  $i$ . Thus, the power of the backscattered signal at each BN is determined as,

$$P_{BN_i}^{tx} = \zeta_{BN_i} P_{BN_i}^{rx}. \quad (2.8)$$

Moreover, according to the Shannon capacity formula, the achievable data rate of BN $_i$  can be expressed as

$$R_{BN_i} = B \log_2(1 + \text{SINR}_{BN_i}) \text{ bits/s, for all, } i = 1, \dots, N_l, \quad (2.9)$$

where  $B$  is the allocated bandwidth for BNs to backscatter their data and  $\text{SINR}_{BN_i}$  is the the signal-to-interference-plus-noise ratio (SINR) of BN $_i$  which will be defined in the following section. Depending on whether the BNs have perfect channel state information (CSI) or not, the outage is likely to happen. Hence, in this thesis, we study the both cases including:1) BNs with no CSI knowledge meaning that the outage is likely to happen, 2) BNs with CSI knowledge meaning that there is no outage.

### 2.1.3 Power-Domain NOMA Protocol

In this work, we consider a power-domain NOMA scheme as the uplink MAC protocol. In order for NOMA scheme to be able to successfully decode the incoming signals, the difference of the channel gains on the same spectrum resource must be sufficiently large. Thus, it is assumed that the channel power gains of BNs in each sub-region are distinct and can be ordered based on a fixed order, which is a common assumption in the uplink NOMA scenario. Note that by fixed-order, we mean that there is only one possible way of ordering channel power gains at each sub-region which is determined based on the acquired statistical CSI by the UAV. Also, note that this order will not change until the end of backscattering time since the large scale fading effect remains constant when the BNs and UAV are not moving during this time. Hence, under this assumption, the

product of uplink and downlink channel power gains can be ordered as

$$d_{k_1}^{-2\alpha} h_{k_1}^2 > \dots > d_{k_{N_l}}^{-2\alpha} h_{k_{N_l}}^2, \quad (2.10)$$

where  $k_{(\cdot)} \in \{BN_1, \dots, BN_N\}$  such that  $k_1, \dots, k_{N_l}$  represent the BNs in sub-region  $s_l$ ,  $l = 1, \dots, W$ , and  $N_l$  is the number of BNs in sub-region  $s_l$  such that  $N = \sum_{l=1}^W N_l$ . Moreover, to make the difference of channel gains more pronounced and obtain a diverse set of received powers, all BNs at each sub-region backscatter their data to the UAV simultaneously with different reflection coefficients,

$$1 > \zeta_{k_1} > \dots > \zeta_{k_{N_l}} > 0. \quad (2.11)$$

Note that with fixed-order SIC employed at the UAV, the successful retrieval and decoding of the BNs' signals become possible. In order to assign reflection coefficients to BNs, the following approach is adopted by the UAV: Since the UAV knows the exact location of BNs and also it knows the statistical CSI of each channel before broadcasting the RF carrier signal to the BNs, it assigns the reflection coefficients to the BNs based on the determined fixed-order channel power gains (Eq.(2.10)). Hence, at each sub-region, the UAV assigns the highest reflection coefficient to the BN with the highest channel power gain, i.e.,  $k_1$ , and, in a descending order, assigns the lowest reflection coefficient to the BN with the lowest channel power gain, i.e.,  $k_{N_l}$ . Note that we assume the time for CSI acquisition and assigning reflection coefficients is negligible compared to the backscattering time  $T$ .

The best performance of NOMA scheme is achieved when the data rate of each BN is greater than the target rate  $\hat{R}$ . Thus, we have

$$B \log_2(1 + \text{SINR}_{k_i}) \geq \hat{R}, \text{ for all } i = 1, \dots, N_l, \quad (2.12)$$

This implies that SINR for each one of the backscattered signals at the UAV is greater than a given SINR threshold  $\gamma$  necessary for successful decoding. Hence,

$$\text{SINR}_{k_1} = \frac{GP_u \zeta_{k_1} h_{k_1}^2 d_{k_1}^{-2\alpha}}{\sum_{j=2}^{N_l} GP_u \zeta_{k_j} h_{k_j}^2 d_{k_j}^{-2\alpha} + \mathcal{N}} \geq \gamma, \quad (2.13)$$

$$\text{SINR}_{k_2} = \frac{GP_u \zeta_{k_2} h_{k_2}^2 d_{k_2}^{-2\alpha}}{\sum_{j=3}^{N_l} GP_u \zeta_{k_j} h_{k_j}^2 d_{k_j}^{-2\alpha} + \mathcal{N}} \geq \gamma, \quad (2.14)$$

⋮

$$\text{SINR}_{k_{N_l}} = \frac{GP_u \zeta_{k_{N_l}} h_{k_{N_l}}^2 d_{k_{N_l}}^{-2\alpha}}{\mathcal{N}} \geq \gamma, \quad (2.15)$$

where  $\gamma = 2^{\frac{\hat{R}}{B}} - 1$  and  $\mathcal{N}$  is the noise power. Note that the backscattered signal by  $k_1$  is the strongest signal at each sub-region and gets decoded at the UAV first; on the other hand,  $k_{N_l}$ 's signal is considered to be the weakest one and gets decoded after all the stronger signals are decoded.

#### 2.1.4 UAV Mobility Model

In order to improve the number of successfully decoded bits, the UAV may need to lower its altitude to get closer to BNs. Hence, only a portion of the target area can be illuminated by the RF carrier signal, and the target area is divided into  $W$  sub-regions as given in FIGURE 2.1. Consequently, the total flight time will be divided into  $W$  sub-slots. Furthermore, the UAV's trajectory plan is modeled as: Given the number of sub-regions  $W$  which is obtained at any altitude and beamwidth value as discussed above, the UAV moves from the origin of each sub-region as its 2-D location over each sub-region, i.e.,  $(x, y)$ , to adjacent sub-region as illustrated in FIGURE 2.1. Note that the 2-D location of the UAV over each sub-region is assumed to be the origin point of each sub-region. According to (2.3), since we assume that the flying time from each origin to adjacent one is negligible compared to the flight time over each sub-region, it does not matter from which sub-region the UAV starts to hover.

## 2.2 Problem Formulation

Our objective is to maximize the total number of successfully decoded bits while minimizing its flight time, by finding the optimal UAV altitude  $H^*$  and beamwidth  $\theta^*$ , and backscattering reflection coefficients  $\zeta_i^*$ ,  $i = 1, \dots, N_l$ . Note that by finding optimal  $H$  and  $\theta$ , the optimal number of sub-regions  $W^*$  and the trajectory plan of the UAV are also obtained. Let the network throughput  $C(\theta, H, \zeta_1, \dots, \zeta_{N_l})$  be the ratio of the total number of successfully decoded bits during all time sub-slots (i.e., in all sub-regions) to the total flight time:

$$C(\theta, H, \zeta_1, \dots, \zeta_{N_l}) = \frac{\sum_{l=1}^{W(\theta, H)} \sum_{i=1}^{N_l} C_i(\theta, H, \zeta_1, \dots, \zeta_{N_l})}{T_f(\theta, H)}, \quad (2.16)$$

where  $C_i(\theta, H, \zeta_1, \dots, \zeta_{N_l})$  is the number of successfully decoded bits of BN  $k_i$  at sub-region  $s_l$ ,  $l = 1, \dots, W$ . Depending on whether the BNs have perfect CSI knowledge or not,  $C_i(\theta, H, \zeta_1, \dots, \zeta_{N_l})$  is defined as follows:

- **BNs Without CSI Knowledge:** In this case, we need to consider the outage probability since it is possible that the achievable backscattering rate is less than

the target rate; hence, we have

$$C_i(\theta, H, \zeta_1, \dots, \zeta_{N_l}) = T\hat{R}(1 - P_{out,k_i}^{(s_i)}(\theta, H, \zeta_1, \dots, \zeta_{N_l})), \quad (2.17)$$

where  $P_{out,k_i}^{(s_i)}(\theta, H, \zeta_1, \dots, \zeta_{N_l})$  where  $i = 1, \dots, N_l$ , is the outage probability corresponding to BN  $k_i$ , which is determined as<sup>1</sup>

$$P_{out,k_1}^{(s_1)} = 1 - \Pr(\text{SINR}_{k_1}^{(s_1)} \geq \gamma), \quad (2.18)$$

$$P_{out,k_2}^{(s_2)} = 1 - \Pr(\text{SINR}_{k_1}^{(s_1)} \geq \gamma, \text{SINR}_{k_2}^{(s_2)} \geq \gamma), \quad (2.19)$$

$\vdots$

$$P_{out,k_{N_l}}^{(s_{N_l})} = 1 - \Pr(\text{SINR}_{k_1}^{(s_1)} \geq \gamma, \dots, \text{SINR}_{k_{N_l}}^{(s_{N_l})} \geq \gamma), \quad (2.20)$$

By using (2.10), (2.11) and (2.13), we have

$$\begin{aligned} GP_u \zeta_{k_1} h_{k_1}^2 d_{k_1}^{-2\alpha} &\geq GP_u \zeta_{k_2} h_{k_2}^2 d_{k_2}^{-2\alpha} \gamma \\ &+ \gamma \sum_{j=3}^{N_l} GP_u \zeta_{k_j} h_{k_j}^2 d_{k_j}^{-2\alpha} + \gamma \mathcal{N} \\ &\approx \gamma \sum_{j=3}^{N_l} GP_u \zeta_{k_j} h_{k_j}^2 d_{k_j}^{-2\alpha} + \gamma \mathcal{N}. \end{aligned} \quad (2.21)$$

This approximation holds due to the distinct channel power gains and reflection coefficients as stated in (2.11) and (2.13), respectively. Consequently,  $GP_u \zeta_{k_1} h_{k_1}^2 d_{k_1}^{-2\alpha} \gg GP_u \zeta_{k_2} h_{k_2}^2 d_{k_2}^{-2\alpha} \gamma$  assuming  $\gamma \leq 1$ , and thus,  $GP_u \zeta_{k_2} h_{k_2}^2 d_{k_2}^{-2\alpha}$  has infinitesimal effect on  $\Pr(\text{SINR}_{k_1} \geq \gamma)$  compared to  $\gamma \sum_{j=3}^{N_l} GP_u \zeta_{k_j} h_{k_j}^2 d_{k_j}^{-2\alpha}$ . Hence, the events  $\text{SINR}_{k_1} \geq \gamma$  and  $\text{SINR}_{k_2} \geq \gamma$  are approximately independent. The same argument can be applied to argue that

$$\Pr(\text{SINR}_{k_i} \geq \gamma | \text{SINR}_{k_{i'}} \geq \gamma) \approx \Pr(\text{SINR}_{k_i} \geq \gamma), \quad (2.22)$$

for any  $i < i'$  where  $i \geq 2$ . Therefore, (2.18)-(2.20) can be approximated as

$$P_{out,k_i}^{(s_i)} \approx 1 - \prod_{j=1}^i \Pr(\text{SINR}_{k_j}^{(s_j)} \geq \gamma), \text{ for all } i = 1, \dots, N_l. \quad (2.23)$$

Define  $z_i = \zeta_{k_i} h_{k_i}^2 d_{k_i}^{-2\alpha}$ ,  $i = 1, \dots, N_l$ , which is a log-normal distributed random variable since the product of two log-normal distributed random variables is also log-normal with mean  $\mu_{z_i} = \ln(\zeta_{k_i} d_{k_i}^{-2\alpha})$  and variance  $\sigma_{z_i}^2 = 4a^2\sigma^2$  where  $a = \frac{\ln 10}{10}$ .

<sup>1</sup>In order to simplify the notation, from now on we will not show the  $(\theta, H, \zeta_1, \dots, \zeta_{N_l})$  dependence explicitly; for instance, we will use  $C$  instead of  $C(\theta, H, \zeta_1, \dots, \zeta_{N_l})$ .

Then, we have from (2.13)

$$\Pr(\text{SINR}_{k_i}^{(s_i)} \geq \gamma) = \Pr\left(\frac{z_i}{\sum_{j=i+1}^{N_l} z_j + \frac{N}{GP_u}} \geq \gamma\right). \quad (2.24)$$

To make the problem tractable, we assume that the thermal noise is negligible and it is only taken into account when there is no interference (i.e., in calculating the SINR of the weakest BN at each sub-region  $\text{SINR}_{k_{N_l}}$ ). Thus

$$\Pr(\text{SINR}_{k_i}^{(s_i)} \geq \gamma) = \begin{cases} \Pr\left(\frac{z_i}{\sum_{j=i+1}^{N_l} z_j} \geq \gamma\right), & \text{for all } i \neq N_l, \\ \Pr\left(\frac{z_i}{\frac{N}{GP_u}} \geq \gamma\right), & \text{for all } i = N_l. \end{cases} \quad (2.25)$$

The distribution of  $\sum_{j=i+1}^{N_l} z_j$  has no closed-form expression, but it can be reasonably approximated by another log-normal distribution  $A_i$  at the right tail. Its probability density function at the neighborhood of 0 does not resemble any log-normal distribution. In the following section, we will discuss a well-known approximation method to approximate this distribution.

**Theorem 2.1. (Fenton-Wilkinson (FW) Approximation)** *A random variable  $U$  is log-normal, i.e.  $U \sim \text{LN}(\mu, \sigma^2)$ , if and only if  $\ln(U) \sim N(\mu, \sigma^2)$ . A log-normal random variable has PDF*

$$f_U(u) = \frac{1}{u\sqrt{2\pi\sigma^2}} \exp\left(-\frac{(\ln u - \mu)^2}{2\sigma^2}\right), \quad u > 0, \quad (2.26)$$

for any  $\sigma^2 > 0$ . The expected value of  $U$   $E(U) = \exp(\mu + 0.5\sigma^2)$  and the variance of  $U$  is  $\text{Var}(U) = (\exp(\sigma^2) - 1)\exp(2\mu + \sigma^2)$ . If  $U \sim \text{LN}(\mu, \sigma^2)$ , then  $bU \sim \text{LN}(\mu + \ln(b), \sigma^2)$  where  $b > 0$ . Conveniently, then, we can find a PDF for a  $U \sim \text{LN}(\mu, \sigma^2)$  as a convolution of  $X \sim \text{LN}(0, \sigma^2)$  as follows:

$$f_U(u) = (1/\exp(\mu)) \cdot f_X((1/\exp(\mu)) \cdot u) \quad (2.27)$$

Consider the sum of  $Q$  i.i.d. log-normal random variables,  $U$ , such that  $U = U_1 + U_2 + \dots + U_q$  where each  $U_q \sim \text{LN}(\mu_{U_q}, \sigma_{U_q}^2)$  with the expected value and variance described above. The expected value and variance of  $U$  are  $E(U) = Q \cdot E(U_q)$  and  $\text{Var}(U) = Q \cdot \text{Var}(U_q)$ . The FW approximation is a log-normal PDF with parameters  $\mu_U$  and  $\sigma_U^2$  such that  $\exp(\mu_U + 0.5\sigma_U^2) = Q \cdot E(U_q)$  and  $(\exp(\sigma_U^2) - 1) \cdot \exp(2\mu_U + \sigma_U^2) = Q \cdot \text{Var}(U_q)$ . Solving for  $\mu_U$  and  $\sigma_U^2$  gives

$$\mu_U = \ln(Q \cdot \exp(\mu_{U_q})) + 0.5(\sigma_{U_q}^2 - \sigma_U^2), \quad (2.28)$$

and

$$\sigma_U^2 = \ln\left(\frac{\exp(\sigma_U^2) - 1}{Q} + 1\right). \quad (2.29)$$

Hence, using the aforementioned FW method, the following approximation for the distribution of  $\sum_{j=i+1}^{N_l} z_j$  is obtained by matching the mean and variance of another log-normal distribution as

$$\mu_{A_i} = \ln \left[ \sum_{j=i+1}^{N_l} e^{\mu_{z_j} + \frac{\sigma_{z_j}^2}{2}} \right] - \frac{a^2 \sigma_{A_i}^2}{2}, \quad (2.30)$$

$$\sigma_{A_i}^2 = \ln \left[ \frac{\sum_{j=i+1}^{N_l} e^{(2\mu_{z_j} + \sigma_{z_j}^2)} (e^{\sigma_{z_j}^2} - 1)}{(\sum_{j=i+1}^{N_l} e^{\mu_{z_j} + \frac{\sigma_{z_j}^2}{2}})^2} + 1 \right]. \quad (2.31)$$

Thus,  $\text{SINR}_{BN(\cdot)}^{(s_l)}$  can be approximated by a log-normal random variable defined as  $Y_{BN(\cdot)}^{(s_l)}$  with mean  $\mu_{Y(\cdot)}$  and variance  $\sigma_{Y(\cdot)}^2$ , which can be calculated as

$$\mu_{Y_i} = \begin{cases} \mu_{z_i} - \mu_{A_i}, & \text{for all } i \neq N_l, \\ \mu_{z_i} - \ln\left(\frac{N}{GP_u}\right), & \text{for all } i = N_l, \end{cases} \quad (2.32)$$

and

$$\sigma_{Y_i}^2 = \begin{cases} \sigma_{z_i}^2 + a^2 \sigma_{A_i}^2, & \text{for all } i \neq N_l, \\ \sigma_{z_i}^2, & \text{for all } i = N_l. \end{cases} \quad (2.33)$$

Hence, the outage probability corresponding to sub-region  $s_l$  can be determined as

$$\begin{aligned} P_{out, k_i}^{(s_l)} &\approx 1 - \prod_{j=1}^i \Pr(Y_{k_j}^{(s_l)} \geq \gamma) \\ &= 1 - \prod_{j=1}^i \left[ \frac{1}{2} - \frac{1}{2} \operatorname{erf}\left(\frac{10 \log_{10}(\gamma) - \mu_{Y_j}}{\sigma_{Y_j} \sqrt{2}}\right) \right], \text{ for all } i = 1, \dots, N_l \end{aligned}$$

- **BNs With Perfect CSI Knowledge:** In this case, the number of successfully decoded bits of BN  $k_i$  at sub-region  $s_l$  is expressed as

$$C_i = TB \log_2(1 + \text{SINR}_{k_i}^{(s_l)}), \quad (2.34)$$

### 2.2.1 Optimization Problem

Finally, the optimization problem can be expressed as follows where we aim to maximize the network throughput by jointly finding an optimal resource allocation policy, UAV altitude, and beamwidth,

$$\max_{\theta, H, \zeta_{k_1}, \dots, \zeta_{k_{N_l}}} C \quad (2.35a)$$

$$\text{s.t. } H_{min} \leq H \leq H_{max}, \quad (2.35b)$$

$$\theta_{min} \leq \theta \leq \theta_{max}, \quad (2.35c)$$

$$\zeta_{k_{N_l}} < \dots < \zeta_{k_1}, \text{ for all } l = 1, \dots, W \quad (2.35d)$$

$$0 < \zeta_{k_i} < 1, \text{ for all } i = 1, \dots, N_l. \quad (2.35e)$$

In this thesis, we assume that the backscattering reflection coefficients are pre-defined and given such that they are allocated as

$$\begin{aligned} \zeta_{k_{N_l}} &= \zeta_{min}, \\ \zeta_{k_{N_l-1}} &= \zeta_{min} + \frac{(\zeta_{max} - \zeta_{min})}{N_l - 1}, \\ \zeta_{k_{N_l-2}} &= \zeta_{min} + \frac{2(\zeta_{max} - \zeta_{min})}{N_l - 1}, \\ &\vdots \\ \zeta_{k_1} &= \zeta_{max}, \end{aligned} \quad (2.36)$$

for all  $l = 1, \dots, W$ , and  $0 < \zeta_{min} < \zeta_{max} < 1$ ,

where  $\zeta_{min}$  and  $\zeta_{max}$  are the reflection coefficients assigned to the weakest and strongest BN, respectively. Hence, the optimization problem is expressed as

$$\max_{\theta, H} C \quad (2.37a)$$

$$\text{s.t. } H_{min} \leq H \leq H_{max}, \quad (2.37b)$$

$$\theta_{min} \leq \theta \leq \theta_{max}, \quad (2.37c)$$

(2.35) is a fractional programming (FP) problem with non-differentiable fractional objective function; hence, the problem is intractable. We noticed that in this case, it is very challenging to even approximate the problem with a convex problem. Since the cardinality of the set of altitudes and beamwidths that a UAV can hover over are finite, and the locations of BNs are known a priori, we use exhaustive search method to determine the optimal UAV altitude and beamwidth for a pre-defined given set of backscattering reflection coefficients.

TABLE 2.1: Simulation Parameters

Parameter	Value
Density of BNs ( $\rho$ )	1 BNs/m <sup>2</sup>
UAV transmit power ( $P_u$ )	20 dBm
Bandwidth ( $B$ )	10 MHz
Noise power ( $\mathcal{N}$ )	-70 dBm
Radius of target area ( $R_{cov}$ )	100 m
SINR threshold ( $\gamma$ )	-10 dB
Path-loss exponent ( $\alpha$ )	2.7
Altitude range ( $H$ )	[10, 60] m
Beamwidth range ( $\theta$ )	[20, 90] <sup>o</sup>
Reflection coefficient range ( $\zeta$ )	[0.1, 0.99]
Log-normal shadowing variance ( $\sigma^2$ )	9 dB

## 2.3 Simulation Results

In this section, we evaluate the throughput  $C$  with respect to the UAV altitude and beamwidth of the UAV for the case that BNs have no perfect CSI knowledge, under various considerations of network parameters including the SINR threshold  $\gamma$  and backscattering reflection coefficients. We also analyze the effect of the density of BNs on the ground, on the throughput. Moreover, the dependency of the network throughput on the number of BNs is investigated for two different channel thresholds. The outage performance of three strongest BNs at each sub-region, i.e.,  $k_1$ ,  $k_2$ , and  $k_3$ , is also evaluated with respect to the number of BNs in each sub-region. Unless otherwise stated, in all experiments we use the parameters given in TABLE 2.1. In FIGURE 2.3, the throughput is plotted with respect to  $H$  for  $\gamma = -11.5$ ,  $-10.5$ , and  $-10$  dB. The figure illustrates that with lower SINR thresholds, there exists an optimal altitude where the throughput is maximized, and as the sensitivity of the SIC decoder at the UAV increases, the throughput increases as well. When the altitude is high, the number of BNs backscattering is also high, but the received power from each backscatter signal is small. This in turn reduces the probability of correct decoding. However, if the altitude is low, then even if there are fewer incoming transmissions from the BNs, the total flight time of the UAV is high, reducing the throughput. In FIGURE 2.3, we also examine the performance of the network throughput with respect to UAV's altitude  $H$  with different BN reflection coefficients. The figure shows that the way the reflection coefficients are selected has a significant impact on the throughput (the network parameters used for FIGURE 2.3 are given in TABLE 2.1). When the reflection coefficients assigned to BNs

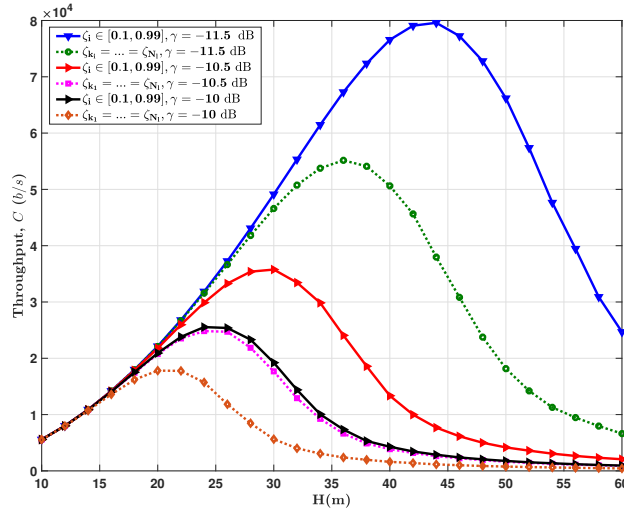


FIGURE 2.3: Throughput performance with respect to UAV altitude  $H$ , for two different ways of selecting the selection of reflection coefficients  $\zeta$  and for three different SINR thresholds  $\gamma$  ( $\theta = 60^\circ$ ,  $\rho = 1$  BNs/m<sup>2</sup>).

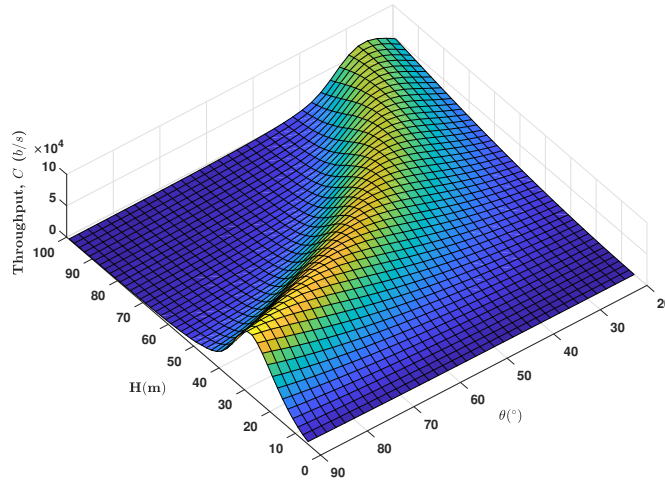


FIGURE 2.4: Throughput performance with respect to the beamwidth  $\theta$  and altitude  $H$  ( $\gamma = -11.5$  dB,  $\rho = 1$  BNs/m<sup>2</sup>).

at each sub-region are in the range  $[0.1, 0.99]$  with equal intervals, i.e.,

$$\zeta_{k_{N_l}} = 0.1, \zeta_{k_{N_l-1}} = 0.1 + \frac{(0.99 - 0.1)}{N_l - 1}, \zeta_{k_{N_l-2}} = 0.1 + \frac{2(0.99 - 0.1)}{N_l - 1}, \dots, \zeta_{k_1} = 0.99, \quad (2.38)$$

$$\forall l = 1, \dots, W,$$

the throughput improves by more than 40% compared to the case when all the reflection coefficients are the same, for  $\gamma = -11.5$  dB. When the reflection coefficient values are apart from each other, the received powers of the backscattered signals get further apart,

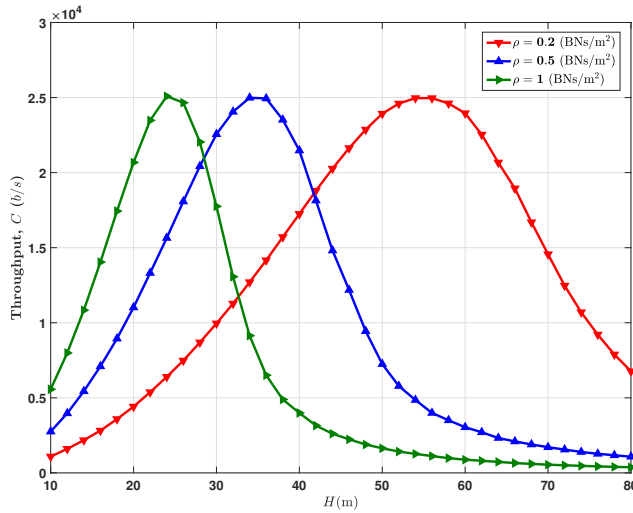


FIGURE 2.5: Throughput performance with respect to UAV altitude  $H$ , for three different density of BNs  $\rho$  on the target area ( $\gamma = -10.5$  dB,  $\theta = 60^\circ$ ).

and thus, the SIC decoder makes fewer decoding errors. Note that when  $\zeta_{k_1} = \dots = \zeta_{k_{N_l}}$ , the actual values of  $\zeta_{k_{(i)}}$  does not matter due to the fact that, when the background noise is omitted in (16), the  $\zeta_{k_{(i)}}$  values in the numerator and denominator will cancel each other.

Furthermore, in FIGURE 2.4, we evaluate the performance of the network throughput with respect to the beamwidth  $\theta$ , and altitude  $H$ . The figure implies that there exists an optimal set of beamwidth and altitude where the throughput is maximized. To be more precise, the maximum throughput is achieved when the UAV operates with its highest beamwidth,  $\theta = 45^\circ$ , and at an altitude  $H = 27$  m since in this case more number of BNs can be served at a lower altitude which means lower path-loss effect. It can also be seen that at any fixed beamwidth (or altitude), there is always an optimal altitude (or beamwidth) at which the throughput is maximized. In FIGURE 2.5, we examine how the density  $\rho$  of BNs on the target area can effect the optimal altitude where the throughput is maximized. When the density is  $\rho = 1$  BNs/m<sup>2</sup>, the optimal altitude is  $H^* = 24$  m. However, as the density gets lower to  $\rho = 0.2$  BNs/m<sup>2</sup>, in order to achieve the same maximum throughput, the UAV needs to operate at a higher altitude  $H^* = 54$  m covering more BNs. Moreover, in FIGURE 2.7, we evaluate the effect of the number of BNs covered at each sub-region  $N_l$  on the network throughput under two different SINR thresholds  $\gamma = -10.5$  and  $-10$  dB. We observe that when the UAV operates with a fixed beamwidth, there exists an optimal average number of BNs that can be covered by the UAV in each sub-region such that the network throughput is maximized. Also, when a lower SINR threshold is employed, approximately 260 more BNs can be served in each sub-region at the optimal altitude where the network throughput is maximized.

Finally, in FIGURE 2.7, we investigate the dependency of the outage probability

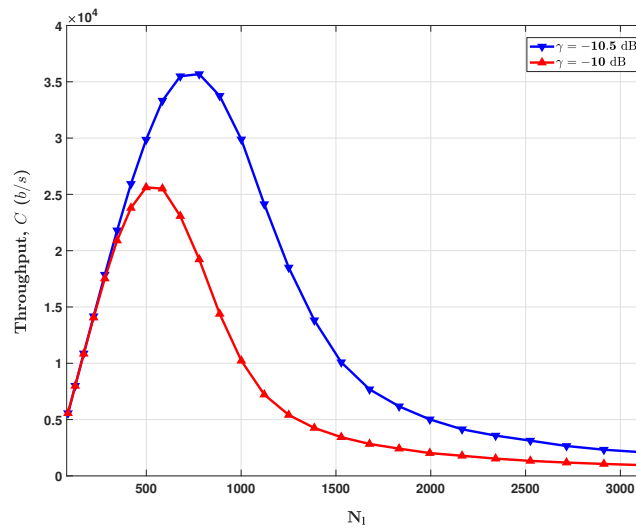


FIGURE 2.6: Throughput performance with respect to the number BNs at each sub-region  $N_l$  ( $\theta = 60^\circ$ ,  $\rho = 1$  BNs/m<sup>2</sup>).

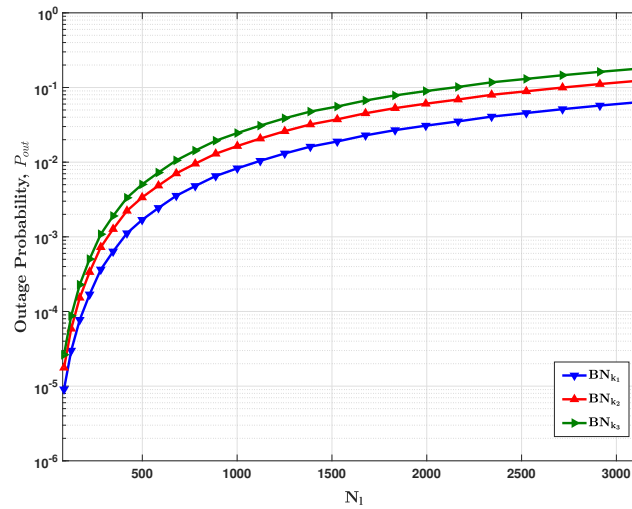


FIGURE 2.7: Outage performance of three strong BNs  $\theta$  with respect to the number BNs at each sub-region  $N_l$  ( $\gamma = -10$  dB,  $\theta = 60^\circ$ ,  $\rho = 1$  BNs/m<sup>2</sup>).

of three strong BNs in each sub-region  $k_1, k_2$ , and  $k_3$  such that  $d_{k_1}^{-2\alpha} h_{k_1}^2 > d_{k_2}^{-2\alpha} h_{k_2}^2 > d_{k_3}^{-2\alpha} h_{k_3}^2$ . The figure states that as the UAV moves to a higher altitude, and thus, covers more number of BNs in each sub-region, the outage probability of decoding the data bits of each BN increases monotonically which is due to a significant increase in amount of interference and path-loss effect. Also, it shows that the outage performance of the strongest BN, i.e.,  $k_1$ , is always better than weaker BNs since it has a better channel chain with the highest reflection coefficient compared to other BNs, it gets decoded first which is independent of decoding of other BNs. This figure shows that when the number of BNs at each sub-region is  $N_l = 170$ , the outage probability of the strongest BN is

$P_{out,k_1} < 10^{-4}$  which means that the SIC decoder can decode the backscatter signal of BN  $k_1$  with very a low probability of error assuming that  $\gamma = -10$  dB.

## Chapter 3

# Data Collection in Hybrid Terrestrial and Aerial NOMA Backscatter Networks

In chapter 2, we discussed a backscatter wireless network where the data collector and RF transmitter are co-located at the UAV. In this chapter, however, we consider a separate data collector and RF carrier emitter such that the former is a gateway on the ground and the latter is a single UAV hovering over the target area. The system model, problem formulation, and numerical results are discussed in the following sections.

### 3.1 System Model

As shown in Fig. 3.1, in this scenario, we consider a single-cell UAV-assisted NOMA backscatter network where  $M$  backscatter nodes (BNs) are distributed independently and uniformly (i.e., binomial point process) in a area of size  $\mathcal{A}$  m<sup>2</sup> with density  $\rho = \frac{M}{\mathcal{A}}$  BNs/m<sup>2</sup> and different from the previous work, there is a single UAV acting only as a mobile power transmitter, and there is a separate data collector (DC) located on the ground in order to collect data from BNs. Similar to previous work, we assume that the UAV is equipped with a directional antenna with adjustable beamwidth  $\theta$  and it hovers over the target area for a fixed duration while continuously broadcasting a single carrier RF signal with fixed power  $P_u$  to all BNs on the ground. On the ground side, the BNs become active and employ the received RF signal to backscatter their data to DC simultaneously based on power-domain NOMA scheme.

Furthermore, we assume that the coverage area of the UAV when it hovers at altitude

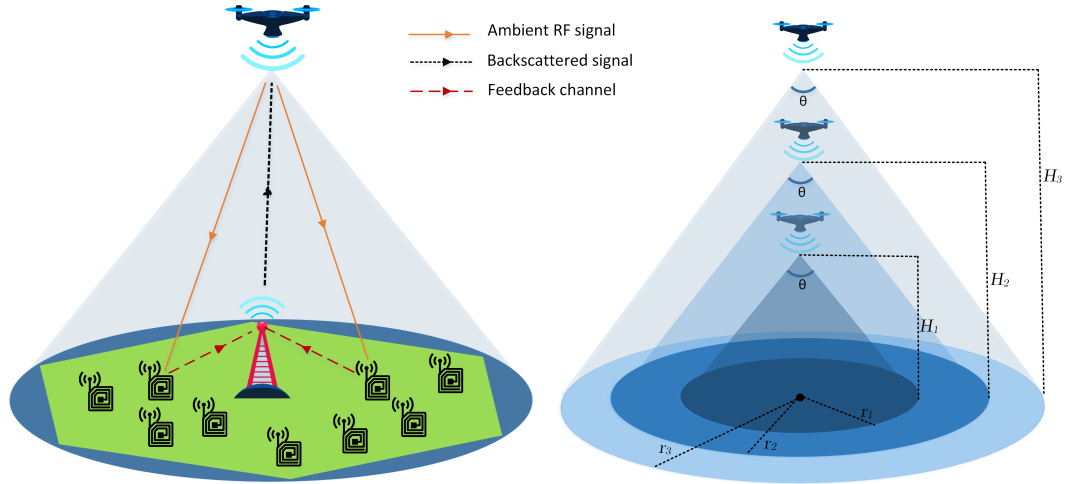


FIGURE 3.1: System Model.

$H$  with beamwidth  $\theta$  is a circle with radius  $r = H \tan \frac{\theta}{2}$ . Thus, the average number of BNs covered by the UAV is given by

$$N = \frac{3\sqrt{3}}{2} \rho H^2 \tan^2 \frac{\theta}{2}. \quad (3.1)$$

Moreover, by receiving the RF signal from the UAV, the BNs map their data bits to the received RF signal and then backscatter them to the UAV, simultaneously, for a fixed time duration  $T$ .

For simplicity, we also assume that the azimuth and elevation half-power beamwidths of the UAV antenna are equal, which are both denoted as  $\theta$ , with  $\theta \in (0, \frac{\pi}{2})$ . Moreover, the corresponding antenna gain in direction  $(\Theta, \Phi)$  is approximately modeled same as that of in chapter 2, Eq. (2.4).

### 3.1.1 Channel Model

The channel between the UAV and BN  $i$  is modeled by free-space path-loss model as  $d_{BN_i}^{-2}$ , where  $d_{BN_i}$  denotes the distance between the UAV and BN  $i$  determined as

$$d_{BN_i} = \sqrt{H^2 + (x_{BN_i} - x)^2 + (y_{BN_i} - y)^2}, \quad (3.2)$$

where  $x_{BN_i}$  and  $y_{BN_i}$  are the coordinates of BN  $i$  and  $(x, y, H)$  is the 3-D coordinate of UAV over the target area. Moreover, the channel power gain of the link between the DC and BN  $i$  is denoted by  $\hat{d}_{BN_i}^{-2} |h_{BN_i}|$ , where  $\hat{d}_{BN_i}^{-2}$  denotes the free-space path-loss for

the  $BN_i$  located  $\hat{d}_{BN_i}$  away from the DC which is calculated as

$$\hat{d}_{BN_i} = \sqrt{(x_{BN_i} - x_{DC})^2 + (y_{BN_i} - y_{DC})^2}, \quad (3.3)$$

where  $(x_{DC}, y_{DC})$  represents the coordinates of the DC. Furthermore,  $|h_{BN_i}|$  represents the small scale Rayleigh fading channel power gain such that  $\sqrt{h_{BN_i}}$  follows a complex Gaussian distribution with zero mean and unit variance.

Hence, the received power at  $BN_i$ ,  $P_{BN_i}^{tx}$ , can be written as Eq.(2.6). Let  $\zeta_{BN_i}$  be the reflection coefficient of  $BN_i$  for the purpose of backscattering signal to the DC. Since all the BN are transmitting simultaneously on the same spectrum, thus the power of the backscattered signal of  $BN_i$  is determined as

$$P_{BN_i}^{tx} = \zeta_{BN_i} \hat{d}_{BN_i}^{-2} |h_{BN_i}| P_{BN_i}^{tx}, \text{ for all } i = 1, \dots, N, \quad (3.4)$$

Note that similar to chapter 2, we also assume that the data rate for each BN is the Shannon-rate Eq.(2.12).

Let  $u_{BN_i} = \zeta_{BN_i} \hat{d}_{BN_i}^{-2} |h_{BN_i}| P_{BN_i}^{tx}$  to denote the instantaneous channel power gain of the link between UAV-to- $BN_i$ -to-DC where  $i = 1, \dots, N$ . Then, the random variable  $u_{BN_i}$  is exponentially distributed with parameter  $\lambda_{BN_i}$ . Hence, the probability density function (PDF) of  $u_{BN_i}$  can be formulated as

$$f_{u_{BN_i}}(v) = \lambda_{BN_i} e^{-\lambda_{BN_i} v}, \text{ for all } i = 1, \dots, N, \quad (3.5)$$

where

$$\lambda_{BN_i} = \frac{1}{\mathbb{E}[u_{BN_i}]}, \quad (3.6)$$

where  $\mathbb{E}[\cdot]$  represents the expected value. In the following section, we discuss the problem formulation and the power-domain NOMA scheme as employed in this work.

## 3.2 Problem Formulation

### 3.2.1 NOMA Protocol

Similar to chapter 2, in this work, we also consider a power domain NOMA scheme as the uplink MAC protocol. However, in this chapter, we consider two different SIC decoding schemes according to the order of the channel power gains including dynamic-order and fixed-order, based on the large-scale term (i.e., the average path-loss) and

small-scale term (i.e., Rayleigh fading) of the received power of each BN, respectively. In the following two section, we discuss these approaches in details.

### 3.2.2 Dynamic-ordered Channel Power Gains

For the dynamic-ordered channel power gains, the channel state information (CSI) is assumed to be perfectly known at the DC and accordingly, the UAV. Before the decoding, the DC determines the decoding order based on the instantaneous received signal power of each BN. The instant decoding order can be represented by a permutation denoted by  $\psi$ . According to this order  $\psi$ , the BNS are decoded in sequence of  $[\psi_{k_1}, \psi_{k_2}, \dots, \psi_{k_N}]$  with the instantaneous channel power gain relation:

$$d_{\psi_{k_1}}^{-2} \hat{d}_{\psi_{k_1}}^{-2} |h_{\psi_{k_1}}| > \dots > d_{\psi_{k_N}}^{-2} \hat{d}_{\psi_{k_N}}^{-2} |h_{\psi_{k_N}}|, \quad (3.7)$$

where  $k_{(\cdot)} \in \{BN_1, \dots, BN_N\}$  and  $\psi_{k_{(\cdot)}}$  represents the BN  $k_{(\cdot)}$  under the decoding order  $\psi$ . When decoding the signal of the BN  $\psi_{k_i}$ ,  $i = (1, \dots, N)$ , the SIC receiver should first decode all the prior stronger  $(i - 1)$  BNs' signals, then after subtracting those strong signals from the superimposed received signal, the signal of the BN  $k_i$  get decoded. Note that, the rest of  $(N - i)$  BNs' signals are regarded as the interference. By applying the dynamic-ordered decoding scheme, the instant decoding order can be determined by the instantaneous received signal power of each BN.

On the other hand, to make the difference of channel gains more significant and improve the performance of NOMA scheme, all active BNs backscatter their data to the DC simultaneously with different reflection coefficients. In order to assign reflection coefficients to BNs, the following approach is adopted by the UAV: Upon receiving the BNs' CSI and accordingly, the decoding order  $\psi$ , from the DC through the feedback channel, the UAV assigns the backscattering reflection coefficients in the following order:

$$1 > \zeta_{\psi_{k_1}} > \dots > \zeta_{\psi_{k_N}} > 0, \quad (3.8)$$

hence,

$$u_{\psi_{k_1}} > \dots > u_{\psi_{k_N}}. \quad (3.9)$$

This order implies that the highest reflection coefficient is assigned to the BN with the highest instantaneous channel power gain, i.e.,  $\psi_{k_1}$ . On the other hand, the lowest coefficient is assigned to the BN  $\psi_{k_N}$  which has the lowest instantaneous channel power gain. In this chapter, we assume that the BNs have no CSI knowledge; Hence, since the channel condition may get worse and the received SINR at the DC may be lower than the decoding threshold, the outage is more likely to happen. Hence, we first define

the received SINR of the BN  $k_i$ ,  $i = 1, \dots, N$ , given the channel power gain order (or decoding order)  $\psi$ , i.e.,  $\psi_{k_i}$ , as follows

$$\text{SINR}_{k_1|\psi} = \frac{u_{\psi_{k_1}}}{\sum_{j=2}^N u_{\psi_{k_j}} + \mathcal{N}}, \quad (3.10)$$

$$\text{SINR}_{k_2|\psi} = \frac{u_{\psi_{k_2}}}{\sum_{j=3}^N u_{\psi_{k_j}} + \mathcal{N}}, \quad (3.11)$$

⋮

$$\text{SINR}_{k_N|\psi} = \frac{u_{\psi_{k_N}}}{\mathcal{N}}. \quad (3.12)$$

Based on these received SINR values each BN, the corresponding outage probabilities can be formulated as

$$P_{out,k_1|\psi} = 1 - \Pr(B \log_2(1 + \text{SINR}_{k_1|\psi}) \geq \hat{R}), \quad (3.13)$$

$$P_{out,k_2|\psi} = 1 - \Pr(B \log_2(1 + \text{SINR}_{k_1|\psi}) \geq \hat{R}, B \log_2(1 + \text{SINR}_{k_2|\psi}) \geq \hat{R}), \quad (3.14)$$

⋮

$$P_{out,k_N|\psi} =$$

$$1 - \Pr(B \log_2(1 + \text{SINR}_{k_1|\psi}) \geq \hat{R}, B \log_2(1 + \text{SINR}_{k_2|\psi}) \geq \hat{R}, \dots, B \log_2(1 + \text{SINR}_{k_N|\psi}) \geq \hat{R}). \quad (3.15)$$

Note that given the channel power gain order  $\psi$ , the signal received from of the BN  $k_1$  is the strongest one and gets decoded first at the DC. On the other hand, the signal received from of the BN  $k_N$  is the weakest and gets decoded after all BNs' signal decoded. Based on the following Lemma 1, we can reasonably approximate the conditional outage probability of the BN  $k_i$ .

*Lemma 1.* The outage probability of the BN  $k_i$  under a given decoding order  $\psi$  is determined as

$$P_{out,k_i|\psi} \approx 1 - \prod_{j=1}^i \Pr(\text{SINR}_{k_j|\psi} \geq \gamma), \text{ for all } i = 1, \dots, N, \quad (3.16)$$

where  $\gamma = 2^{\frac{\hat{R}}{B}} - 1$  and  $B$  is the allocated bandwidth to BNs.

*Proof.* Given the the channel power gain order  $\psi$ , the backscattered signal of BN  $k_1$  is successfully decoded at the DC when  $u_{\psi_{k_1}} \geq \gamma u_{\psi_{k_2}} + \gamma \sum_{j=3}^N u_{\psi_{k_j}} + \gamma \mathcal{N}$ . Due to the distinct channels power gains and reflection coefficients stated in (3.7) and (3.8), respectively, we have  $u_{\psi_{k_1}} \gg \gamma u_{\psi_{k_2}}$ . Thus,  $u_{\psi_{k_2}}$  has infinitesimal effect on  $\Pr(\text{SINR}_{k_1|\psi} \geq \gamma)$  compared to  $\sum_{j=3}^N u_{\psi_{k_j}} + \gamma \mathcal{N}$ . Therefore, the events  $\text{SINR}_{k_1|\psi} \geq \gamma$  and  $\text{SINR}_{k_2|\psi} \geq \gamma$  are

approximately independent. The same argument can be applied to argue that

$$\Pr(\text{SINR}_{k_i|\psi} \geq \gamma | \text{SINR}_{k_{i'}|\psi} \geq \gamma) \approx \Pr(\text{SINR}_{k_i|\psi} \geq \gamma), \quad (3.17)$$

for any  $i < i'$  where  $i, i' = 1, \dots, N$ . Hence, the conditional outage probability of the BN  $k_i$  can be approximated as Eq.(3.16).  $\square$

The channel power gain order (or decoding order) can change with the instantaneous received power at the DC. Hence, if we define  $\Psi$  as the set of all possible channel power gain orders when the dynamic-ordered SIC receiver is considered, the outage probability of  $k_i$  can be calculated as

$$P_{out,k_i} = \sum_{\psi \in \Psi} P_\psi P_{out,k_i|\psi}, \text{ for all } i = 1, \dots, N, \quad (3.18)$$

where  $P_\psi$  is the probability of the channel power gain order  $\psi$  which is given by the following Lemma 2.

*Lemma 2.* The probability of the decoding order  $\psi$  in the set of all possible decoding order  $\Psi$  is determined as

$$P_\psi = \frac{\prod_{i=2}^N \lambda_{\psi_{k_i}}}{\prod_{i=2}^N (\sum_{j=1}^i \lambda_{\psi_{k_j}})}. \quad (3.19)$$

*Proof.* As discussed earlier, according to the dynamic-ordered approach, when the order is  $\psi$ , the instantaneous channel power gains are ordered in the sequence as Eq.(3.7). Hence, the decoding order probability can be derived as below

$$\begin{aligned} P_\psi &= \int \cdots \int f(u_{\psi_{k_1}}, u_{\psi_{k_2}}, \dots, u_{\psi_{k_N}}) du_{\psi_{k_1}} du_{\psi_{k_2}} \cdots du_{\psi_{k_N}} \\ &= \int_0^\infty \lambda_{\psi_{k_N}} e^{-\lambda_{\psi_{k_N}} u_{\psi_{k_N}}} du_{\psi_{k_N}} \times \cdots \times \int_{u_{\psi_{k_3}}}^\infty \lambda_{\psi_{k_2}} e^{-\lambda_{\psi_{k_2}} u_{\psi_{k_2}}} du_{\psi_{k_2}} \times \int_{u_{\psi_{k_2}}}^\infty \lambda_{\psi_{k_1}} e^{-\lambda_{\psi_{k_1}} u_{\psi_{k_1}}} du_{\psi_{k_1}} \\ &= \frac{\prod_{i=2}^N \lambda_{\psi_{k_i}}}{\prod_{i=2}^N (\sum_{j=1}^i \lambda_{\psi_{k_j}})}. \end{aligned} \quad (3.20)$$

$\square$

Following the definition of the conditional probability, we can write

$$\Pr(\text{SINR}_{k_i|\psi} \geq \gamma) = \frac{\Pr(\text{SINR}_{\psi_{k_i}} \geq \gamma, \psi)}{P_\psi}. \quad (3.21)$$

To make the problem tractable, we assume that the thermal noise is negligible and it is only taken into account when there is no interference (i.e., in calculating the SINR

of the weakest BN:  $\text{SINR}_{k_N|\psi}$ ). Thus, when  $i = N$ , i.e., the last decoded BN, Eq.(3.21) can be calculated as

$$\begin{aligned} \Pr(\text{SINR}_{k_N|\psi} \geq \gamma) &= \Pr(u_{\psi_{k_N}} > \gamma\mathcal{N}, u_{\psi_{k_1}} > \dots > u_{\psi_{k_N}}) \\ &= \int_{\gamma\mathcal{N}}^{\infty} \lambda_{\psi_{k_N}} e^{-\lambda_{\psi_{k_N}} u_{\psi_{k_N}}} du_{\psi_{k_N}} \times \dots \times \int_{u_{\psi_{k_2}}}^{\infty} \lambda_{\psi_{k_1}} e^{-\lambda_{\psi_{k_1}} u_{\psi_{k_1}}} du_{\psi_{k_1}} \\ &= \frac{\prod_{j=2}^N (\lambda_{\psi_{k_j}}) e^{-(\sum_{j=1}^N \lambda_{\psi_{k_j}}) \gamma\mathcal{N}}}{\prod_{j=2}^N \sum_{t=1}^j \lambda_{\psi_{k_t}}}. \end{aligned} \quad (3.22)$$

On the other hand, when  $i \neq N$ , we have

$$\Pr(\text{SINR}_{\psi_{k_i}} \geq \gamma, \psi) = \Pr(u_{\psi_{k_i}} \geq \gamma \sum_{j=i+1}^N u_{\psi_{k_j}}, \psi). \quad (3.23)$$

Depending on the value of the SINR threshold  $\gamma$ , we can find the joint probability as follows

- **When  $\gamma \geq 1$ :**

In this case, the probability of  $\Pr(u_{\psi_{k_i}} \geq \gamma \sum_{j=i+1}^N u_{\psi_{k_j}}, \psi)$  can be calculated based on the following Lemma 3.

*Lemma 3.* When  $\gamma \geq 1$ , the solution of the joint probability

$\Pr(u_{\psi_{k_i}} \geq \gamma \sum_{j=i+1}^N u_{\psi_{k_j}}, \psi)$  is given by

$$\begin{aligned} \Pr(u_{\psi_{k_i}} \geq \gamma \sum_{j=i+1}^N u_{\psi_{k_j}}, \psi) &= \\ &= \frac{\prod_{j=2}^N \lambda_{\psi_{k_j}}}{\prod_{j=2}^i (\sum_{t=1}^j \lambda_{\psi_{k_t}}) \prod_{j=i+1}^N (\sum_{t=i+1}^j \lambda_{\psi_{k_t}} + (j-i)\gamma \sum_{m=1}^i \lambda_{\psi_{k_m}})}. \end{aligned} \quad (3.24)$$

*Proof.* When  $\gamma \geq 1$ , we can claim that  $\gamma \sum_{j=i+1}^N u_{\psi_{k_j}} > u_{\psi_{k_{i+1}}}$  always holds since the both hand sides are positive and  $\sum_{j=i+1}^N u_{\psi_{k_j}} > u_{\psi_{k_{i+1}}}$ . Hence, based on this inequality and the given channel power gain order  $\psi$ , i.e.,  $u_{\psi_{k_1}} > \dots > u_{\psi_{k_N}}$ , the joint probability can be determined as

$$\begin{aligned}
 & \Pr(u_{\psi_{k_i}} \geq \gamma \sum_{j=i+1}^N u_{\psi_{k_j}}, \psi) \\
 &= \int \cdots \int f(u_{\psi_{k_1}}, \dots, u_{\psi_{k_i}}, u_{k_{i+1}}, u_{\psi_{k_{i+2}}}, \dots, u_{\psi_{k_N}}) du_{\psi_{k_1}} \cdots du_{\psi_{k_N}} \\
 &= \int_0^\infty \lambda_{\psi_{k_N}} e^{-\lambda_{\psi_{k_N}} u_{\psi_{k_N}}} du_{\psi_{k_N}} \times \cdots \times \int_{u_{\psi_{k_{i+2}}}^\infty} \lambda_{\psi_{k_{i+1}}} e^{-\lambda_{\psi_{k_{i+1}}} u_{\psi_{k_{i+1}}}} du_{\psi_{k_{i+1}}} \\
 &\quad \times \int_{\sum_{j=i+1}^N u_{\psi_{k_j}}^\infty} \lambda_{\psi_{k_i}} e^{-\lambda_{\psi_{k_i}} u_{\psi_{k_i}}} du_{\psi_{k_i}} \times \cdots \times \int_{u_{\psi_{k_2}}^\infty} \lambda_{\psi_{k_1}} e^{-\lambda_{\psi_{k_1}} u_{\psi_{k_1}}} du_{\psi_{k_1}}
 \end{aligned} \tag{3.25}$$

□

• **When  $\gamma < 1$ :**

In this case, the joint probability  $\Pr(u_{\psi_{k_i}} \geq \gamma \sum_{j=i+1}^N u_{\psi_{k_j}}, \psi)$  seems to be difficult to solve and thus, finding a closed-form expression for the outage probability is a difficult task. Hence, in this work, we only consider the case when  $\gamma \geq 1$ ; however, as an extension of this work, in the future work, we will aim to consider this case as well.

### 3.2.3 Fixed-order Channel Power Gains

According to this approach, the SIC receiver at the DC decodes the BNs' signals in a fixed order which is determined by only considering the statistical CSI meaning that the BNs' channel power gains are ordered based on their distance to the UAV and DC, i.e.,

$$\hat{d}_{k_1}^{-2} d_{k_1}^{-2} > \hat{d}_{k_2}^{-2} d_{k_2}^{-2} > \cdots > \hat{d}_{k_N}^{-2} d_{k_N}^{-2} \tag{3.26}$$

where  $k_1$  is assumed to have the shortest distance from the UAV-to-BN-to-DC; hence, its backscattered signal is strongest and gets decoded first at the DC. On the other hand, the signal received from  $k_N$  is considered to be the weakest since the distance of UAV-to-BN-to-DC is the longest for  $k_N$ . In this scheme also, the reflection coefficients are assigned to the BNs based on the similar approach discussed for the dynamic-ordered scheme. By receiving the BNs' statistical CSI from the DC through the feedback channel, the UAV assigns the backscattering reflection coefficients in the following order:

$$1 > \zeta_{k_1} > \cdots > \zeta_{k_N} > 0, \tag{3.27}$$

where the highest reflection coefficient is assigned to the BN  $k_1$  and the lowest coefficient is assigned to the BN  $k_N$  which have the lowest and highest average path-loss affect, respectively.

In order to find a closed-form expression for the outage probability of BN  $k_i$  when the decoding order is fixed, we first define the received SINR of BNs at the DC as follows

$$\text{SINR}_{k_1} = \frac{u_{k_1}}{\sum_{j=2}^N u_{k_j} + \mathcal{N}}, \quad (3.28)$$

$$\text{SINR}_{k_2} = \frac{u_{k_2}}{\sum_{j=3}^N u_{k_j} + \mathcal{N}}, \quad (3.29)$$

⋮

$$\text{SINR}_{k_N} = \frac{u_{k_N}}{\mathcal{N}}. \quad (3.30)$$

Then, we have

$$\Pr(\text{SINR}_{k_i} \geq \gamma) = \Pr(u_{k_i} \geq \gamma \sum_{j=i+1}^N u_{k_j} + \gamma \mathcal{N}). \quad (3.31)$$

To make the problem tractable, we assume that the thermal noise is negligible and it is only taken into account when there is no interference (i.e., in calculating the SINR value of the weakest BN,  $(\Pr(\text{SINR}_{k_N} \geq \gamma))$ ). Hence, Eq.(3.31) can be written as

$$\Pr(\text{SINR}_{k_i} \geq \gamma) = \begin{cases} \Pr(u_{k_i} \geq \gamma \sum_{j=i+1}^N u_{k_j}), & i \neq N \\ \Pr(u_{k_i} \geq \gamma \mathcal{N}), & i = N, \end{cases} \quad (3.32)$$

where

$$\begin{aligned} \Pr(u_{k_i} \geq \gamma \sum_{j=i+1}^N u_{k_j}) &= \int_0^\infty \lambda_{k_N} e^{-\lambda_{k_N} u_{k_N}} du_{k_N} \times \cdots \times \int_{\gamma(\sum_{j=i+1}^N u_{k_j})}^\infty \lambda_{k_i} e^{-\lambda_{k_i} u_{k_i}} du_{k_i} \\ &= \prod_{j=i+1}^N \left( \frac{1}{1 + \gamma \frac{\lambda_{k_i}}{\lambda_{k_j}}} \right), \end{aligned} \quad (3.33)$$

and

$$\Pr(u_{k_N} \geq \gamma \mathcal{N}) = \int_{\gamma \mathcal{N}}^\infty \lambda_{k_N} e^{-\lambda_{k_N} u_{k_N}} du_{k_N} = e^{-\lambda_{k_N} \gamma \mathcal{N}}. \quad (3.34)$$

### 3.2.4 Optimization Problem

In this chapter, our objective is to maximize the total average number of successfully decoded bits by the UAV by finding an optimal UAV altitude  $H^*$  and beamwidth  $\theta^*$ .

TABLE 3.1: Simulation Parameters

Parameter	Value
Density of BNs ( $\rho$ )	0.1 BNs/m <sup>2</sup>
UAV transmit power ( $P_u$ )	20 dBm
Noise power ( $\mathcal{N}$ )	-70 dBm
Bandwidth ( $B$ )	10 MHz
SINR threshold ( $\gamma$ )	-7 dB, 0 dB
Altitude range ( $H$ )	[10, 40] m
Beamwidth range ( $\theta$ )	[20, 90] <sup>o</sup>
Reflection coefficient range ( $\zeta$ )	[0.1, 0.99]

Note that by finding optimal  $H^*$  and  $\theta^*$ , the optimal number of BNs  $N^*$  that are served by the UAV can be achieved. Hence, we define the network throughput  $C(\theta, H)$  as the average number of successfully decoded bits per second (i.e., the average sum rate)

$$C(\theta, H) = \sum_{i=1}^{N(\theta, H)} \hat{R}(1 - P_{out, k_i}(\theta, H)). \quad (3.35)$$

Hence, based on the closed-form expression derived for the outage probability of  $k_i$  either in the case of considering dynamic or fixed ordered decoding approaches discussed in the previous section, the optimization problem can be formulated as

$$\max_{\theta, H} C \quad (3.36)$$

s.t.

$$H_{min} \leq H \leq H_{max}, \quad (3.37)$$

$$\theta_{min} \leq \theta \leq \theta_{max}. \quad (3.38)$$

Note that (3.36) is a non-convex problem and since the cardinality of the set of altitudes and beamwidths that a UAV can hover over is finite, and the locations of BNs are known a priori, we use exhaustive search method to determine the optimal solution.

### 3.3 Numerical Results

In this section, we analyze the throughput  $C$  performance of the proposed single cell UAV-assisted NOMA backscatter network with UAV altitude  $H$  and beamwidth  $\theta$  for both fixed and dynamic-ordered channel power gains. We also examine the dependency of the throughput on the selection of backscattering reflection coefficients  $\zeta$  and SINR threshold  $\gamma$ . The outage performance of the stronger BNs including  $k_1, k_2, k_3$ , is also

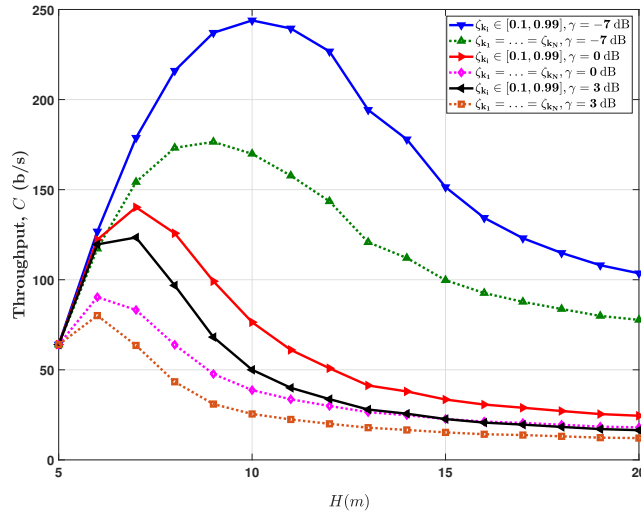


FIGURE 3.2: Throughput Performance considering fixed-ordered decoding scheme with respect to the UAV altitude  $H$ .

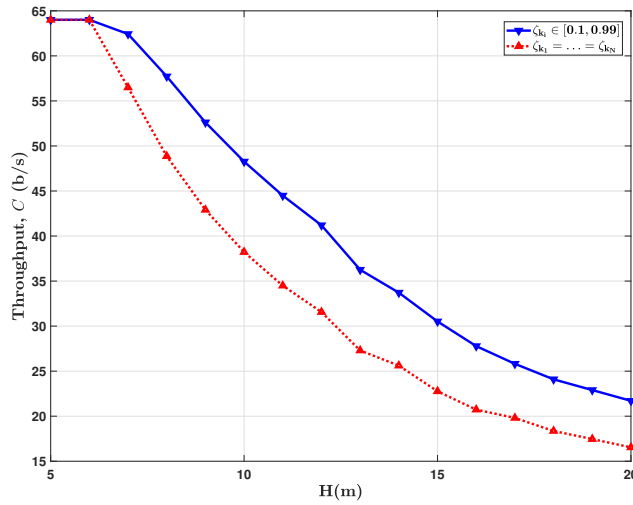


FIGURE 3.3: Throughput performance considering dynamic-ordered decoding scheme with respect to the UAV altitude  $H$  ( $\gamma = 0$  dB).

investigated with respect to the number of BNs  $N$ . Unless otherwise stated, in all experiments we use the parameters given in TABLE 3.1.

In FIGURE 3.2, the throughput is plotted with respect to  $H$  considering the fixed-ordered decoding scheme for  $\gamma = -7, 0$ , and  $3$  dB. The figure illustrates that with lower SINR thresholds, there exists an optimal UAV altitude where the throughput is maximized, and as the sensitivity of the SIC decoder at the DC increases, the throughput increases as well. As the altitude is high, the number of BNs  $N$  backscattering is also high, but the received power from each are close. This reduces the probability of correct decoding. However, if the altitude is low, there are fewer incoming transmissions from

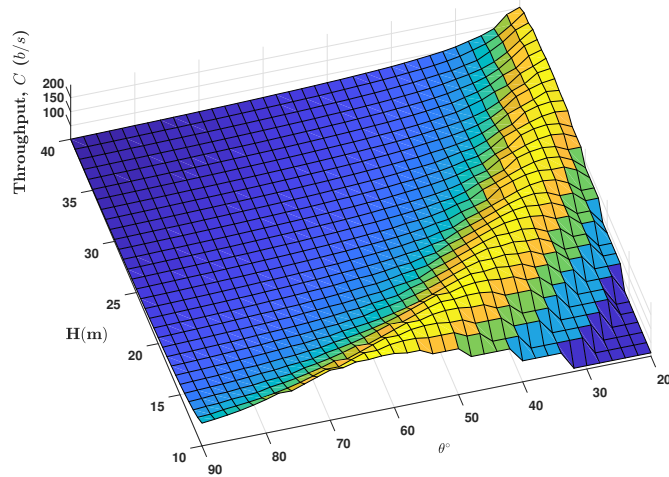


FIGURE 3.4: Throughput performance considering fixed-ordered decoding scheme respect to the UAV altitude  $H$  and beamwidth  $\theta$ . ( $\gamma = -7$  dB).

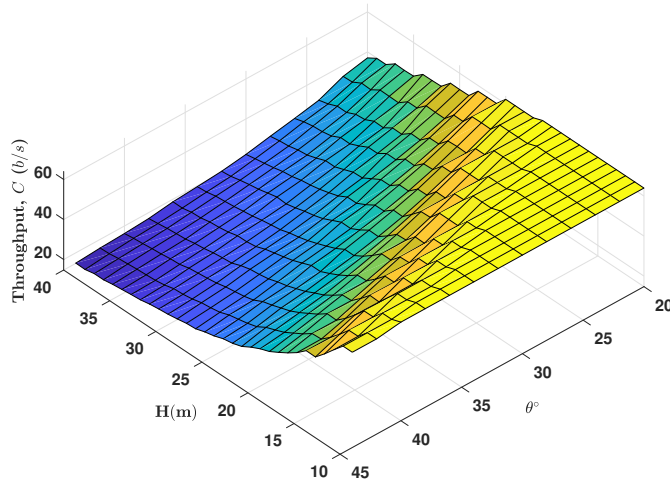


FIGURE 3.5: Throughput performance considering dynamic-ordered decoding scheme respect to the UAV altitude  $H$  and beamwidth  $\theta$  ( $\gamma = 0$  dB).

the BNs reducing the throughput. In FIGURE 3.2, we also investigate the performance of the network throughput with respect to UAV altitude  $H$  with different BN reflection coefficients. Similar to the results of chapter 2, the figure shows that the way the reflection coefficients are selected has a significant impact on the throughput. When the reflection coefficients assigned to the BNs are in the range  $[0.1, 0.99]$  with equal intervals (i.e.,  $\zeta_{k_N} = 0.1, \zeta_{k_{N-1}} = 0.1 + \frac{(0.99-0.1)}{N-1}, \zeta_{k_{N-2}} = 0.1 + \frac{2(0.99-0.1)}{N-1}, \dots, \zeta_{k_1} = 0.99$ ), the throughput improves by more than 40% compared to the case when all the reflection coefficients are the same, for  $\gamma = -7$  dB. When the reflection coefficient values are apart from each other, the received powers of the backscattered signals get further apart, and

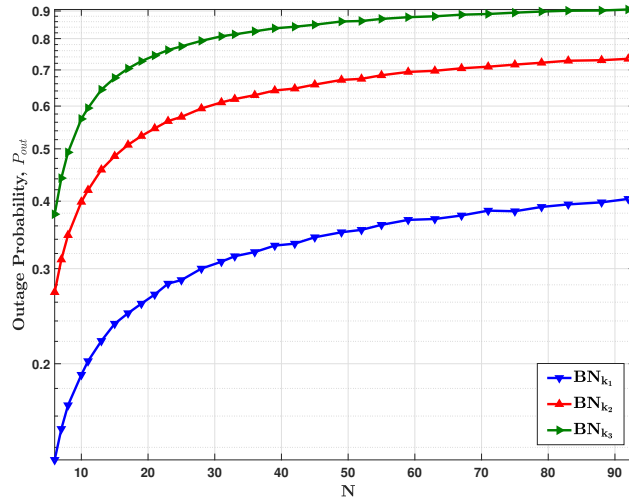


FIGURE 3.6: Outage performance of three most strong BNs considering fixed-ordered decoding scheme, with respect to the number BNs  $N$  ( $\gamma = -7$  dB).

thus, the SIC decoder makes fewer decoding errors. Note that when  $\zeta_{k_1} = \dots = \zeta_{k_N}$ , the actual values of  $\zeta_{k_{(\cdot)}}$  does not matter due to the fact that, when the background noise is omitted in Eq.(3.33), the  $\zeta_{k_{(\cdot)}}$  values will cancel each other.

Similarly, in FIGURE 3.3, we investigate the performance of throughput with respect to UAV altitude  $H$  when the dynamic-ordered decoding scheme is considered. It can be seen that in this case, as the UAV moves to higher altitudes, the throughput decreases monotonically. This is because the number of BNs increase as altitude increase and since the SINR threshold employed at the SIC receiver requires to be more than 0 dB, the SIC receiver decodes correctly. Hence, we observe that to achieve a high performance in the backscatter networks which usually operate in low powers (in this work: 20 dB), with far away and separate receiver (the DC) and RF carrier emitter (the UAV), utilizing SIC decoders lower SINR thresholds is very critical. FIGURE 3.3 also shows that by using reflection coefficients apart from each other, similar to the case discussed above, the throughput improves due to the same reason as discussed above for fixed-ordered case.

Furthermore, in FIGURE 3.4 and 3.5, we evaluate the performance of the network throughput with respect to the beamwidth  $\theta$ , and altitude  $H$  for both fixed and dynamic-ordered decoding schemes, respectively. The figure implies that there exists an optimal set of beamwidth and altitude where the throughput is maximized. To be more precise, in FIGURE 3.4, it can also be seen that at any fixed beamwidth (or altitude), there is always an optimal altitude (or beamwidth) at which the throughput is maximized. In FIGURE 3.5, when the UAV operates at lower altitudes, the dependency of the throughput on the UAV beamwidth,  $\theta$ , is very low since in this case more number of BNs are served by the UAV, with lower path-loss effect. Hence, when the  $\theta$  is low,

although the number of BNs decrease, the antenna gain increases which surpasses this reduction. On the other hand, when the  $\theta$  is high, we observe a decreases in antenna gain which is surpassed by the increase in the number of BNs. Moreover, to achieve higher throughput when the UAV operates at higher altitudes, the UAV is better to operate with a low beamwidth to overcome the path-loss effect by increasing the antenna gain. The figure states that the sum-rate of NOMA increases as the altitude grows since the number of BNs in the UAV's hovering area increase as well; however, after an optimal altitude, the sum-rate degrades dramatically due to excessive amount of interference and path-loss effect. Moreover, the selection of reflection coefficients can increase the distinction of received powers from BNs improving the NOMA performance. The figure shows that when more BNs are covered, distinct reflection coefficient assignment improves the sum-rate significantly.

Finally, in FIGURE 3.6, the outage performance of three most strong BNs including  $k_1, k_2, k_3$ , is plotted with respect the number of BNs in the target area considering the fixed-orderd decoding scheme. Note that  $k_1$  has the strongest signal and sequentially,  $k_2$  and  $k_3$  have weaker signals. As expected, the outage performance of  $k_1$  is better compared to  $k_1$  and  $k_2$ , since its channel gain is better and get decoded independent of the rest of BNs. Moreover, the high number of BNs which is achieved as the UAV operates in higher altitudes, results in worse outage performance of each BN due to the high path-loss effect and excessive amount of interference.

## Chapter 4

# Data Collection via Over-the-Air Computation in Backscatter Networks

### 4.1 System Model

In this chapter, we propose a UAV mobility-assisted communication framework to tackle the challenge of compensating the channel effect in AirComp systems. To be more precise, a sampling-then-mapping mechanism is introduced such that the UAV first takes samples to obtain the sum of channel gains at different locations and then collects sensed data and computes a linear combination of sensed data. By optimizing the linear coefficients, the UAV aims to improve the mean square error (MSE) performance.

#### 4.1.1 Overall Network Model

As illustrated in FIGURE 4.1, We consider a wireless sensor network with  $N$  backscatter devices distributed independently and uniformly randomly over a circular target area with radius  $R_{cov}$ . Each node is equipped with a single sensor measuring an environmental parameter such as temperature, humidity, atmospheric pressure, etc. The node is equipped with an RF antenna receiving RF signal and then emitting a modulated backscatter signal. The UAV has a collocated bi-static reader and acts both as a data collector and a carrier emitter. UAV employs two separate antennas for transmission and reception operating at different frequency bands to avoid self-interference. UAV follows a given and fixed flight path at an altitude of  $H$  meters, and a finite number,

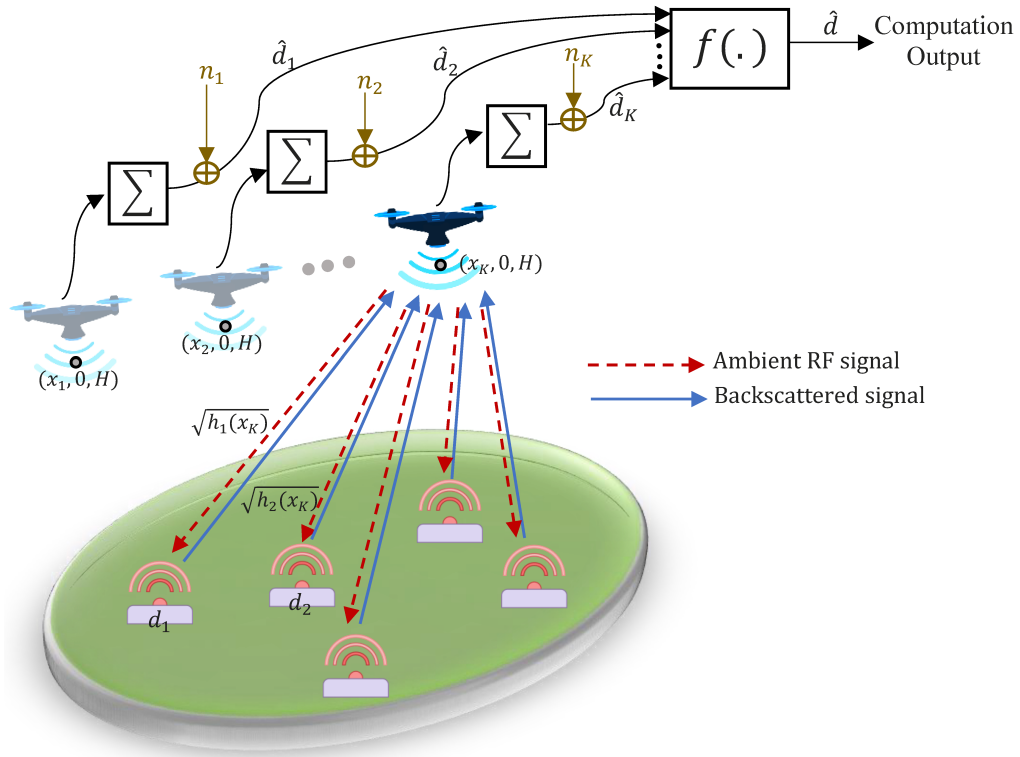


FIGURE 4.1: Network Model.

$K$  of stop-over positions  $(x_k, y_k)$ ,  $k = 1, \dots, K$  over each of which it hovers for a finite duration of time.

In a basic backscatter channel, there are two links: *Forward* (power-up) link from the UAV to a sensor node, and *backscatter* link from the sensor to the UAV. Most air-to-ground channel measurements and statistical models focus on large-scale statistics such as mean path-loss [37]. In this work, we assume that there is no obstruction between the ground sensors and the UAV, and thus, the channels between the sensors and the UAV are assumed to be independent and identically distributed (iid) free-space path-loss channels.

At each stop-over location,  $k$ , UAV broadcasts a carrier signal  $S(t)$ , with power  $P$  over the forward channel, i.e.,

$$S(t) = \Re\{\sqrt{P}e^{j(2\pi f_c t)}\}. \quad (4.1)$$

Let  $B(t)$  be the received signal at sensor  $i$ , i.e.,

$$B_i(t) = \Re\left\{\frac{g_0\sqrt{P}e^{j(2\pi f_c t)}}{D_i(k)} + n(t)\right\}, \quad (4.2)$$

where  $g_0$  is the channel gain at a reference distance 1 m [50],  $D_i(k)$  is the distance between the sensor  $i$  and UAV when it is at location  $k$ , and  $n(t)$  is the additive white

noise. The received power at sensor  $i$  is  $P_{B_i}^k = \frac{g_0^2 P}{D_i^2(k)}$ . Each sensor node reflects a portion of the receiver signal over the backscatter channel. At the UAV, the received signal from sensor  $i$  is

$$Z_i(t) = \Re\left\{\frac{g_0\sqrt{\zeta_i P}e^{j(2\pi f_c t)}}{D_i^2(k)} + n(t)\right\}, \quad (4.3)$$

where  $\zeta_i$  is the backscatter reflection coefficient. The received power is  $P_{Z_i}^k = \left(\frac{g_0\sqrt{P\zeta_i}}{D_i^2(k)}\right)^2$ . In the rest of the letter, we drop the  $t$  notation in order to avoid any confusion.

Hence, the overall channel power gain between the sensor  $i$  and UAV when UAV is at location  $k$ , is

$$h_i(x_k) = \frac{g_0^2}{H^2 + (x_k - x_i)^2 + y_i^2}, \quad i = 1, \dots, N, \quad (4.4)$$

where  $(x_i, y_i)$  is the coordinate of the sensor  $i$ .

#### 4.1.2 Over-the-air functional computation

Over-the-air functional computation uses the summation property of MAC where the sensors transmit simultaneously and coherently such that the receiver obtains a commutable nomographic function of data. In this work, our proposed method is suitable for a polynomial function of observations as the target nomographic function such as the one given as:

$$d = \sum_{i=1}^N w_i d_i^{v_i}, \quad (4.5)$$

where  $w_{(\cdot)}$  and  $v_{(\cdot)}$ , are positive constants.

In conventional applications of Aircomp, the coherent combination of multiple received data in the nomographic function is ensured thanks to the individual transmissions amplified with a precoding gain that is reciprocal of instantaneous channel gain. Here, we do not assume the availability of channel gains, and thus, there is no precoding of the individual sensor transmissions. Instead, we utilize the mobility UAVs to provide a form of channel diversity. Specifically, our proposed Aircomp method has two phases. In the first phase, UAV collects reference signals from multiple stop-over locations. Note that a reference signal collected by the UAV is the sum aggregate of backscatter reflections from all sensor nodes and provides sum channel gains at the respective locations. In the second phase, UAV visits the same locations, but this time each backscatter node

transmits their measured sensor value. The UAV is tasked to combine the measurements made in the second phase by assigning a linear coefficient to each based on its sum channel gain measurements obtained in the first phase.

### 4.1.3 Sampling Phase

In the first phase, UAV takes  $K$  noisy samples at different predefined locations  $(x_k, y_k)$  with a pilot signal, i.e., all backscatter sensors simultaneously transmit a unit value. Hence, at sample location  $k$ , UAV receives  $\sum_{i=1}^N \Re\left\{\frac{g_0\sqrt{P}e^{j(2\pi f_c t)}}{D_i^2(x_k, y_k)} + n'(t)\right\}$ , from which it determines the sum channel gain at location  $k$  as  $\sum_{i=1}^N g_i(x_k, y_k) + n'_k$ , where  $n'_k$  is a Gaussian distributed sampling noise with zero-mean and variance  $\sigma_{n'_k}^2$ , and

$$g_i(x_k, y_k) = \sqrt{\zeta_i P} h_i(x_k, y_k). \quad (4.6)$$

### 4.1.4 Mapping Phase

In the second step, the UAV starts to collect  $K$  samples at the same location  $(x_k, y_k)$  with actual sensor data, i.e.,  $d_i$  for sensor  $i$ ,  $i = 1, \dots, N$ . We assume that sensor data come from a Gaussian source such that  $d_i \sim \mathcal{N}(\mu_{d_i}, \sigma_{d_i}^2)$ . Hence, after coherent and simultaneous transmissions, the sampled data at the UAV at sample  $k$  can be written as

$$\hat{d}_k = \sum_{i=1}^N g_i(x_k, y_k) d_i + n_k, \quad \forall k = 1, \dots, K, \quad (4.7)$$

where  $n_k$  is a zero-mean Gaussian noise with variance  $\sigma_{n_k}^2$ .

**Definition 4.1.** Let define the estimated function  $\hat{d}$  as a function of sampled data as follows

$$\hat{d} = f(\hat{d}_1, \hat{d}_2, \dots, \hat{d}_K), \quad (4.8)$$

where  $f$  is defined as a mapping function in order to perform channel-inversion to compensate the channel effect.

In this work, we consider  $f$  as a linear combination of observations such that

$$\hat{d} = \sum_{k=1}^K \beta_k \left( \sum_{i=1}^N g_i(x_k, y_k) d_i + n_k \right), \quad (4.9)$$

where  $\beta_k, k = 1, \dots, K$ , are positive linear mapping coefficients determined by the UAV. Comparing the target function (4.5) with the estimated one (4.9), the computation error which quantifies the AirComp performance, is measured by the mean-squared-error (MSE) defined as

$$\begin{aligned}
\mathbf{MSE}(d, \hat{d}) &= \mathbf{E}[(\hat{d} - d)^2] \\
&= \sum_{i=1}^N \sigma_{d_i}^2 \left( \sum_{k=1}^K \beta_k g_i(x_k, y_k) \right)^2 + w_i \mathbf{Var}(d_i^{v_i}) \\
&\quad - 2 \left( \sum_{k=1}^K \beta_k g_i(x_k, y_k) w_i \mathbf{E}[d_i^{v_i+1}] \right) \\
&\quad - w_i \mathbf{E}[d_i^{v_i}] \sum_{k=1}^K \beta_k g_i(x_k, y_k) \sigma_{d_i}^2 + \left( \sum_{i=1}^N w_i \mathbf{E}[d_i^{v_i}] \right)^2 + \sum_{k=1}^K \beta_k^2 \sigma_{n_k}^2, \tag{4.10}
\end{aligned}$$

where  $\mathbf{E}[\cdot]$  and  $\mathbf{Var}(\cdot)$  are expected and variance values, respectively. For a special case where  $w_i = 1$  and  $v_i = 1, i = 1, \dots, N$ , the target function becomes the sum of observations and the MSE can be expressed as

$$\begin{aligned}
\mathbf{MSE}(d, \hat{d}) &= \sum_{i=1}^N \sigma_{d_i}^2 \left( \left( \sum_{k=1}^K \beta_k g_i(x_k, y_k) \right)^2 - 2 \left( \sum_{k=1}^K \beta_k g_i(x_k, y_k) w_i \right. \right. \\
&\quad \left. \left. - w_i \mu_{d_i} \sum_{k=1}^K \beta_k g_i(x_k, y_k) \right) + 1 \right) + \left( \sum_{i=1}^N \mu_{d_i} \right)^2 + \sum_{k=1}^K \beta_k^2 \sigma_{n_k}^2. \tag{4.11}
\end{aligned}$$

## 4.2 Problem Formulation

Moreover, since in practical scenarios usually the exact location of sensors are unknown, in this letter, we also assume that only the statistics of the sensor locations are known for the UAV.

Considering the polynomial function of observations (Eq. (4.5)) as the target function, our objective is to minimize MSE, i.e., improving the AirComp performance, by designing optimal linear sampling coefficients  $\beta_k$  for a given UAV trajectory plan  $\{(x_k, y_k)\}_{k=1}^K$ .

Thus, the optimization problem can be formulated as

$$\begin{aligned}
& \min_{\{\beta_k\}_{k=1}^K} \mathbf{E}_{g_i} \left[ \sum_{i=1}^N \sigma_{d_i}^2 \left( \sum_{k=1}^K \beta_k g_i(x_k, y_k) \right)^2 + w_i \mathbf{Var}(d_i^{v_i}) \right. \\
& \quad - 2 \left( \sum_{k=1}^K \beta_k g_i(x_k, y_k) w_i \mathbf{E}[d_i^{v_i+1}] \right. \\
& \quad \left. - w_i \mathbf{E}[d_i^{v_i}] \sum_{k=1}^K \beta_k g_i(x_k, y_k) \sigma_{d_i}^2 \right) + \left( \sum_{i=1}^N w_i \mathbf{E}[d_i^{v_i}] \right)^2 \\
& \quad \left. + \sum_{k=1}^K \beta_k^2 \sigma_{n_k}^2 \right] \tag{4.12a}
\end{aligned}$$

$$\text{s.t. } \sum_{k=1}^K \beta_k \leq \beta_0, \tag{4.12b}$$

where constraint (4.12b) ensures that the sum of linear mapping coefficients does not exceed a upper bound since they are indeed power-type coefficients.

### 4.2.1 Solution of Optimization Problem

It is noticed the problem is not tractable in this form; however, for a special case, the problem is convex such that optimal solution can be calculated according to Theorem 1.

*Theorem 1.* For the case that  $\beta_1 = \dots = \beta_K$ , the optimal solution of Eq. (4.19a) is

$$\beta^* = \frac{\sum_{i=1}^N \sum_{k=1}^K \mathbf{E}[g_i] w_i \mathbf{E}[d_i^{v_i+1}] + \frac{1}{2} w_i \sigma_{d_i}^2 \mathbf{E}[d_i^{v_i}] \sum_{k=1}^K \mathbf{E}[g_i]}{\sum_{i=1}^N \sigma_{d_i}^2 \left( \sum_{k=1}^K \mathbf{Var}(g_i) + \left( \sum_{k=1}^K \mathbf{E}[g_i] \right)^2 \right) + \sum_{k=1}^K \sigma_{n_k}^2}. \tag{4.13}$$

where the channel gain statistics can be determined as  $\mathbf{E}[g_i] = \int g_i f_g(g_i) dg_i$ ,  $\mathbf{Var}(g_i) = \mathbf{E}[g_i^2] - \mathbf{E}[g_i]^2$ .

If the target function is considered as the sum of the observations, i.e.,  $w_i = 1, v_i = 1$ , we have

$$\beta^* = \frac{\sum_{i=1}^N \sigma_{d_i}^2 \sum_{k=1}^K \mathbf{E}[g_i]}{\sum_{i=1}^N \sigma_{d_i}^2 \left( \sum_{k=1}^K \mathbf{Var}(g_i) + \left( \sum_{k=1}^K \mathbf{E}[g_i] \right)^2 \right) + \sum_{k=1}^K \sigma_{n_k}^2}, \tag{4.14}$$

*Proof.* It is noticed that  $\frac{\partial^2 \mathbf{E}_{g_i}[\text{MSE}(\hat{d}-d)]}{\partial \beta^2} \geq 0$ , hence, the problem (4.19a) is a convex problem with respect to  $\beta$  and can be solved by using Lagrangian method. Let  $\mathcal{L}(\beta, \gamma)$

be the Lagrangian function expressed as

$$\begin{aligned}
 \mathcal{L}(\beta, \gamma) &= \sum_{i=1}^N \sigma_{d_i}^2 \beta^2 \mathbf{E}[(\sum_{k=1}^K g_i)^2] + w_i \mathbf{Var}(d_i^{v_i}) \\
 &\quad - 2(\beta w_i \mathbf{E}[d_i^{v_i}] \sum_{k=1}^K \mathbf{E}[g_i] - \beta w_i \mathbf{E}[d_i^{v_i}] \sigma_{d_i}^2 \sum_{k=1}^K \mathbf{E}[g_i]) \\
 &\quad + (\sum_{i=1}^N w_i \mathbf{E}[d_i^{v_i}])^2 + \beta^2 \sum_{k=1}^K \sigma_{n_k}^2 - \gamma(K\beta - \beta_0),
 \end{aligned} \tag{4.15}$$

where  $\gamma$  is the Lagrangian multiplier. Following the KKT conditions, i.e.,

$$\frac{\partial \mathcal{L}(\beta, \gamma)}{\partial \beta} = 0, \tag{4.16}$$

$$\gamma(K\beta - \beta_0) = 0, \tag{4.17}$$

the optimal solution, when  $\gamma = 0$ , can be determined as Eq. (4.13). Note that we also employ the definition of variance,  $\mathbf{Var}(z) = \mathbf{E}[z^2] - \mathbf{E}[z]^2$  to simplify the expression.

## 4.2.2 Heuristic Approach

Due to the high complexity of calculating the expectation over the channel power gains, the problem is not tractable; hence, we introduce a heuristic approach to solve the problem. We assume that at each sampling step, the channel gains can be approximated as follows

$$g_i(x_k, y_k) \approx \frac{\alpha_k}{N}, \forall i, k, \tag{4.18}$$

hence, the optimization problem can be transformed as

$$\begin{aligned}
 \min_{\{\beta_k\}_{k=1}^K} &\sum_{i=1}^N \sigma_{d_i}^2 \left( \sum_{k=1}^K \beta_k \frac{\alpha_k}{N} \right)^2 + w_i \mathbf{Var}(d_i^{v_i}) \\
 &\quad - 2 \left( \sum_{k=1}^K \beta_k \frac{\alpha_k}{N} w_i \mathbf{E}[d_i^{v_i+1}] - w_i \mathbf{E}[d_i^{v_i}] \sum_{k=1}^K \beta_k \frac{\alpha_k}{N} \sigma_{d_i}^2 \right) \\
 &\quad + \left( \sum_{i=1}^N w_i \mathbf{E}[d_i^{v_i}] \right)^2 + \sum_{k=1}^K \beta_k^2 \sigma_{n_k}^2
 \end{aligned} \tag{4.19a}$$

$$\text{s.t. } \sum_{k=1}^K \beta_k \leq \beta_0. \tag{4.19b}$$

Since the problem is convex with respect to  $\beta_k$ , we can use Lagrangian method and apply Karush-Kuhn-Tucker (KKT) conditions to solve this problem and obtain a

sub-optimal solution as

$$\beta_k = \frac{\sum_{i=1}^N w_i \mathbf{E}[d_i^{v_i+1}] - w_i \mathbf{E}[d_i^{v_i}] \sigma_{d_i}^2 - \sum_{k' \neq k}^K \beta_{k'} \frac{\alpha_{k'}}{N} \sum_{i=1}^N \sigma_{d_i}^2}{\frac{\alpha_k}{N} \sum_{i=1}^N \sigma_{d_i}^2 + \frac{N \sigma_{n_k}^2}{\alpha_k}}, \forall k. \quad (4.20)$$

To obtain an independent  $\beta_k$  value, we assume that  $\sum_{k' \neq k} \beta_{k'} \alpha_{k'} = (K-1) \beta_k \alpha_k$ , we have

$$\beta_k = \frac{\sum_{i=1}^N w_i \mathbf{E}[d_i^{v_i+1}] - w_i \mathbf{E}[d_i^{v_i}] \sigma_{d_i}^2}{\frac{\alpha_k}{N} \sum_{i=1}^N \sigma_{d_i}^2 + \frac{N \sigma_{n_k}^2}{\alpha_k} + (K-1) \frac{\alpha_k}{N} \sum_{i=1}^N \sigma_{d_i}^2}, \forall k. \quad (4.21)$$

Moreover, for the case that the linear mapping coefficients are considered to be the same at each sampling step, i.e.,  $\beta_1 = \dots = \beta_K$ , we have

$$\beta = \frac{\sum_{i=1}^N w_i \mathbf{E}[d_i^{v_i+1}] - w_i \mathbf{E}[d_i^{v_i}] \sigma_{d_i}^2}{\frac{1}{N} \sum_{k=1}^K \alpha_k \sum_{i=1}^N \sigma_{d_i}^2 + \frac{N \sum_{k=1}^K \sigma_{n_k}^2}{\sum_{k=1}^K \alpha_k}}, \forall k. \quad (4.22)$$

### 4.3 Simulation Results

In this section, we evaluate the MSE performance considering the sum of observations as the target function, i.e.,  $w_i = 1$ ,  $v_i = 1$ , with respect to the number of samples  $N$  in which the UAV takes along  $x$ -axis, and also the number of backscatter sensors  $K$  covered by the UAV. In FIGURE 4.2, the MSE performance is plotted with respect to  $N$ . The figure illustrates that when the linear mapping coefficients  $\beta_k$ ,  $k = 1, \dots, K$ , are not chosen wisely to compensate the channel effect according to the summation of channel gains and channel statistics, there is around 10 dB reduction in the MSE value compared to the case that no channel inversion is performed. Moreover, as the number of samples  $N$  increases the MSE degrades dramatically and becomes almost fixed after some number of sampling numbers. It is also observed that noise have a significant effect on the performance of MSE such that when  $K = 5$ , there is up to 5 dB reduction in MSE trend. The network parameters that are considered in this experiment are as  $P = 30$  dBm,  $\sigma_n^2 = -70$  dBm,  $H = 4$  m,  $R_{cov} = 4$  m,  $K = 5$ ,  $N = 50$ , and  $\zeta = 0.99$ . Moreover, since backscatter systems mainly operate at  $f = 868$  MHz, we consider  $g_0 = 0.0275$  ( $g_0 = \frac{c}{4\pi f}$ ).

To examine the performance of the MSE with respect to the number of backscatter sensors  $K$ , FIGURE 4.3 is plotted. It can be seen that with the increase of the number of IoT backscatter sensors the decreasing rate of is the same for both of cases where linear mapping coefficients are considered to be equal or are selected individually. The network parameters that are considered in this experiment are as  $P = 30$  dBm,  $\sigma_n^2 = -70$  dBm,  $H = 4$  m,  $R_{cov} = 4$  m,  $K = 5$ ,  $N = 50$ , and  $\zeta = 0.99$ . Moreover, since

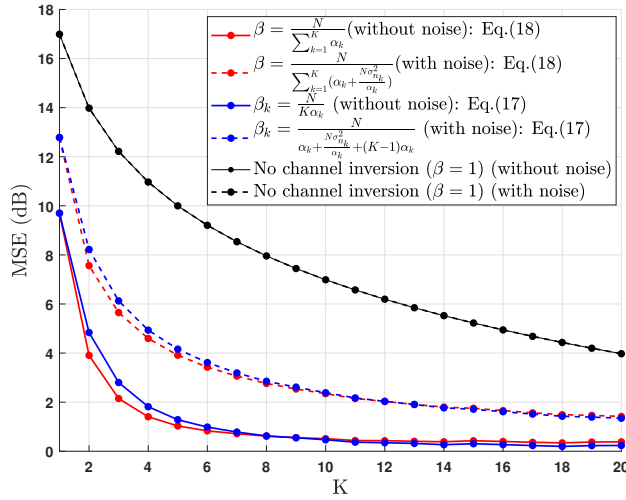


FIGURE 4.2: MSE performance vs. the number of samples  $K$  ( $N = 50$ ,  $g_0 = 0.0275$ ,  $H = 4$  m,  $R_{cov} = 4$  m,  $P = 30$  dBm).

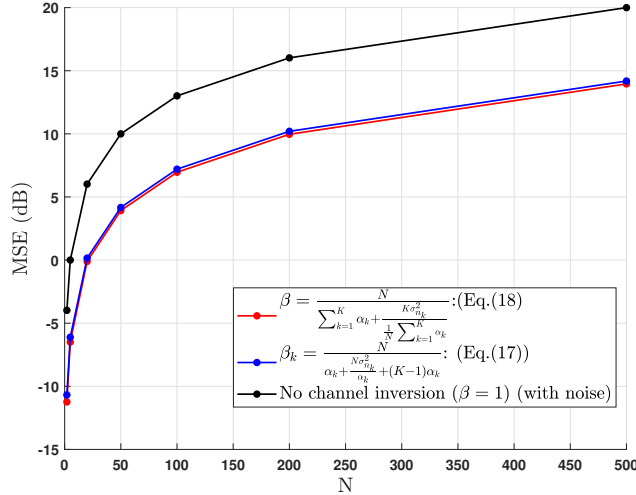


FIGURE 4.3: MSE performance vs. the number of sensors  $N$  ( $K = 5$ ,  $g_0 = 0.0275$ ,  $H = 4$  m,  $R_{cov} = 4$  m,  $P = 30$  dBm).

backscatter systems mainly operate at  $f = 868$  MHz, we consider  $g_0 = 0.0275$  ( $g_0 = \frac{c}{4\pi f}$ ). Furthermore, in FIGURE 4.2 and 4.3, considering the carrier frequency to be  $f = 868$  KHz, we evaluate the MSE performance with respect to the number of samples  $K$  and the number of sensors  $N$ , respectively. The network parameters that are considered in these experiments are as  $P = 20$  dBm,  $\sigma_n^2 = -70$  dBm,  $H = 75$  m,  $R_{cov} = 50$  m,  $K = 5$ ,  $N = 50$ ,  $\zeta = 0.99$ , and  $g_0 = 27.5037$ . It can be seen that when the backscatter sensors operate at lower frequencies, noise has negligible effect on the received signal and accordingly the MSE performance. Moreover, a large area can be also covered by this consideration while UAV hovers at high altitudes.

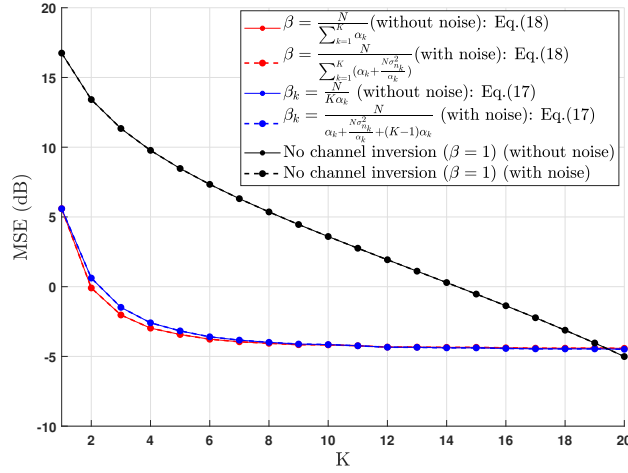


FIGURE 4.4: MSE performance vs. the number of samples  $K$  ( $N = 50$ ,  $g_0 = 27.5037$ ,  $H = 75$  m,  $R_{cov} = 50$  m,  $P = 20$  dBm).

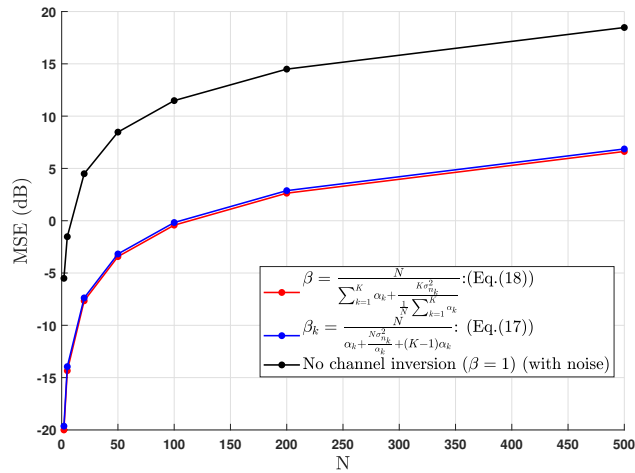


FIGURE 4.5: MSE performance vs. the number of sensors  $N$  ( $K = 5$ ,  $g_0 = 27.5037$ ,  $H = 75$  m,  $R_{cov} = 50$  m,  $P = 20$  dBm).

## Chapter 5

# Summary

The main contributions of this thesis are summarized as following.

In Chapter 2, we develop a framework where the UAV is used as a replacement to conventional terrestrial data collectors in order to increase the efficiency of collecting data from a field of passive backscatter sensors, and simultaneously it acts as a mobile RF carrier emitter to activate backscatter sensors. In the MAC layer, we employ uplink power-domain NOMA scheme to effectively serve a large number of passive backscatter sensors. Our objective is to optimize the path, altitude, and beamwidth of the UAV such that the network throughput is maximized. Moreover, in Chapter 3, we consider a separate data collector and RF carrier emitter such that the former is a gateway on the ground and the latter is a single UAV hovering over the field of backscatter sensors. In both these chapters, an optimization framework is presented to identify the trade-off between numerous network parameters, such as UAV's altitude and beamwidth, number of backscatter devices, and backscatter coefficients. Numerical results show that an optimal altitude and beamwidth is computable for various network setups and that the impact of backscattering reflection coefficients on the maximum network throughput is significant. Based on this optimal altitude and beamwidth, we also show that an optimal trajectory plan is achievable.

In Chapter 4, we utilize the mobility of UAV in order to take sample reference measurements of sum channel gains from a number of different locations. Specifically, a *sample-then-map* mechanism is proposed, wherein UAV takes two flight rounds over the network. In the first round, UAV transmits RF signal and backscatter sensor nodes return back reference values, which in turn provides UAV the sum channel gains at various different locations over the area of coverage. In the second round of flight, UAV transmits RF signal, and this time backscatter nodes return their actual sensor measurements. UAV calculates linear coefficients based on the measured sum channel gains, to minimize the mean square error (MSE) of a linear mapping of the over-the-air-computation

measurements obtained at these various network locations. The performance of the proposed communication mechanism as a simple to implement channel-inversion technique to compensate the channel effect in AirComp systems is analyzed. For polynomial class of functions, a general closed-form expression for the mean squared error (MSE) is also derived. Due to the complexity of the expression, the optimization problem is solved for a special scenario. Moreover, a heuristic approach is also suggested with an acceptable performance. Finally, our results demonstrate that under realistic channel conditions, with a network of 50 sensor nodes, MSE of the proposed scheme is below 2dB, when UAV samples the network at over 12 equally spaced locations.

## Chapter 6

# Conclusions and Future Works

In Chapter 2 and 3, we studied the performance of a novel network model where a NOMA-based long-range backscatter network. Specifically, in Chapter 2, the UAV acts as both aerial power station and data collector where the channels are modeled as path-loss. However, in Chapter 3, the UAV only acts as a power station and a separate ground device is considered for collecting the data. In both Chapter 2 and 3, our objective was to investigate the relationship between the optimal altitude and beamwidth of the UAV and the total number of successfully decoded bits and the UAV's flight time. To the best of the author's knowledge, this is the first work in the literature which studies the UAV-enabled backscatter networks where the objective is to maximize the number of successfully decoded bits while minimizing the flight time by finding the UAV's optimal altitude. The results show that for a selection of parameters, there exist an optimal altitude where the ratio of the number of successfully decoded bits to the flight time is maximized. The limitations of our model include: 1) Availability of perfect location information of BNs; 2) static assignment of reflection coefficients. Moreover, the design framework can also be extended to the multi-UAV scenario, where the UAV-BN association and co-channel interference should be taken into account.

Moreover, in Chapter 4, the major contribution is the introduction of an UAV mobility-assisted sampling-then-mapping mechanism as a simple channel-inversion technique to compensate the channel effect in AirComp systems. The proposed approach improves the AirComp performance significantly in terms of MSE. As a future work, we will consider joint optimization of UAV location, backscattering reflection coefficient allocation, and linear sampling coefficient allocation policies with the aim of minimization of the MSE under UAV mobility and backscattering constraints. Another direction is to aim to find an optimal channel-inversion function such that MSE is minimized.

# Bibliography

- [1] Q. Wu, Y. Zeng, and R. Zhang, "Joint trajectory and communication design for UAV-enabled multiple access," in *Proc. of IEEE Global Communications Conference (Globecom)*, Singapore, Dec. 2017, pp. 1-6.
- [2] I. Bor-Yaliniz and H. Yanikomeroglu, "The new frontier in RAN heterogeneity: Multi-tier drone-cells," *IEEE Communications Magazine*, vol. 54, no. 11, pp. 48-55, Nov. 2016.
- [3] C. Zhan, Y. Zeng, and R. Zhang, "Energy-efficient data collection in UAV enabled wireless sensor network," *IEEE Wireless Communications Letters*, vol. 7, no. 3, pp. 328-331, Jun. 2018.
- [4] J. Gong, T. H. Chang, C. Shen, and X. Chen, "Flight time minimization of UAV for data collection over wireless sensor networks," *IEEE Journal on Selected Areas in Communications* (Early Access), Aug. 2018.
- [5] X. Lu, D. Niyato, H. Jiang, D. I. Kim, Y. Xiao, and Z. Han, "Ambient backscatter assisted wireless powered communications," *IEEE Wireless Communications*, vol. 25, no. 2, pp. 170-177, Apr. 2018.
- [6] W. Liu, K. Huang, X. Zhou, and S. Durrani, "Backscatter communications for internet-of-things: Theory and applications," *arXiv preprint arXiv:1701.07588*, Aug. 2017.
- [7] N. Van Huynh, D. T. Hoang, X. Lu, D. Niyato, P. Wang, and D. I. Kim, "Ambient backscatter communications: A contemporary survey," *IEEE Communications Surveys & Tutorials* (Early Access), May 2018.
- [8] V. Talla, M. Hesar, B. Kellogg, A. Najafi, J. R. Smith, and S. Gollakota, "LoRa backscatter: Enabling the vision of ubiquitous connectivity," in *Proc. of ACM on Interactive, Mobile, Wearable and Ubiquitous Technologies*, vol. 105, pp. 24, Sept. 2017.

- [9] M. Varshney, O. Harms, C. Pérez-Penichet, C. Rohner, F. Hermans, and T. Voigt, “LoRea: A backscatter architecture that achieves a long communication range,” in *Proc. of 15th ACM Conference on Embedded Network Sensor Systems (SenSys)*, New York, USA, 2017, Article 18, 14 pages.
- [10] Z. Ding, X. Lei, G. K. Karagiannidis, R. Schober, J. Yuan, and V. K. Bhargava, “A survey on non-orthogonal multiple access for 5G networks: Research challenges and future trends,” *IEEE Journal on Selected Areas in Communications*, vol. 35, no. 10, pp. 2181-2195, Oct. 2017.
- [11] S. M. R. Islam, N. Avazov, O. A. Dobre, and K. S. Kwak, “Power-domain non-orthogonal multiple access (NOMA) in 5G systems: Potentials and challenges,” *IEEE Communications Surveys & Tutorials*, vol. 19, no. 2, pp. 721-742, Second Quarter 2017.
- [12] Z. Zhang, H. Sun, and R. Q. Hu, “Downlink and uplink non-orthogonal multiple access in a dense wireless network,” *IEEE Journal on Selected Areas in Communications*, vol. 35, no. 12, pp. 2771-2784, Dec. 2017.
- [13] L. Dai, B. Wang, Z. Ding, Z. Wang, S. Chen, and L. Hanzo, “A Survey of Non-Orthogonal Multiple Access for 5G,” *IEEE Communications Surveys and Tutorials*, vol. 20, no. 3, pp. 2294-2323, third quarter 2018.
- [14] K. Higuchi and A. Benjebbour, “Non-orthogonal multiple access (NOMA) with successive interference cancellation for future radio access,” *IEICE Transactions on Communications*, vol. E98.B, no. 3, pp. 403-414, 2015.
- [15] K. W. Choi, A. A. Aziz, D. Setiawan, N. M. Tran, L. Ginting, and D. I. Kim, “Distributed Wireless Power Transfer System for Internet of Things Devices,” *IEEE Internet of Things Journal*, vol. 5, no. 4, pp. 2657-2671, August 2018.
- [16] E. Zihan, K. W. Choi, and D. I. Kim, “Distributed random access scheme for collision avoidance in cellular device-to-device communication,” *IEEE Transactions on Wireless Communication*, vol. 14, no. 7, pp. 3571-3585, July 2015.
- [17] O. Abari, H. Rahul, and D. Katabi, “Over-the-air function computation in sensor networks,” CoRR, vol. abs/1612.02307, pp. 1-8, December 2016. [Online]. Available: <http://arxiv.org/abs/1612.02307>
- [18] B. Nazer and M. Gastpar, “Computation over multiple-access channels,” *IEEE Transactions on Information Theory*, vol. 53, no. 10, pp. 3498-3516, 2007.
- [19] M. Gastpar, “Uncoded transmission is exactly optimal for a simple Gaussian sensor network,” *IEEE Transactions on Information Theory*, vol. 54, no. 11, pp. 5247-5251, November 2008.

- [20] R. Soundararajan and S. Vishwanath, "Communicating linear functions of correlated Gaussian sources over a MAC," *IEEE Transactions on Information Theory*, vol. 58, no. 3, pp. 1853-1860, March 2012.
- [21] J. J. Xiao, S. Cui, Z. Q. Luo, and A. J. Goldsmith, "Linear coherent decentralized estimation," *IEEE Transactions Signal Processing*, vol. 56, no. 2, pp. 757-770, February 2008.
- [22] O. Abari, H. Rahul, D. Katabi, and M. Pant, "Airshare: Distributed coherent transmission made seamless," in *Proc. IEEE Conference on Computer Communications (INFOCOM)*, April 2015, pp. 1742-1750.
- [23] H. He, S. Zhang, Y. Zeng, and R. Zhang, "Joint altitude and beamwidth optimization for UAV-enabled multiuser communications," *IEEE Communications Letters*, vol. 22, no. 2, pp. 344-347, Feb. 2018.
- [24] H. Shakhatreh, A. Khreishah, A. Alsarhan, I. Khalil, A. Sawalmeh, and N. S. Othman "Efficient 3D placement of a UAV using particle swarm optimization," in *Proc. of IEEE 8th International Conference on Information and Communication Systems (ICICS)*, Irbid, Jordan, Apr. 2017, pp. 258-263.
- [25] M. Alzenad, A. El-Keyi, and H. Yanikomeroglu, "3-D placement of an unmanned aerial vehicle base station for maximum coverage of users with different QoS requirements," *IEEE Wireless Communications Letters*, vol. 7, no. 1, pp. 38-41, Feb. 2018.
- [26] R. I. Bor-Yaliniz, A. El-Keyi, and H. Yanikomeroglu, "Efficient 3-D placement of an aerial base station in next generation cellular networks," in *Proc. of IEEE International Conference on Communications (ICC)*, Kuala Lumpur, Malaysia, May 2016, pp. 1-5.
- [27] M. M. Azari, F. Rosas, K. C. Chen, and S. Pollin, "Ultra reliable UAV communication using altitude and cooperation diversity," *IEEE Transactions on Communications*, vol. 66, no. 1, pp. 330-344, Jan. 2018.
- [28] M. F. Sohail, C. Y. Leow, and S. H. Won, "Non-orthogonal multiple access for unmanned aerial vehicle assisted communication," *IEEE Access*, pp. 22716-22727, Apr. 2018.
- [29] J. Guo, X. Zhou, S. Durrani, and H. Yanikomeroglu, "Design of non-orthogonal multiple access enhanced backscatter communication," *IEEE Transactions on Wireless Communications*, vol. 17, no. 10, pp. 6837-6852, Oct. 2018.
- [30] L. Chen, N. Zhao, Y. Chen, F. R. Yu and G. Wei, "Over-the-Air Computation for IoT Networks: Computing Multiple Functions With Antenna Arrays," in *IEEE Internet of Things Journal*, vol. 5, no. 6, pp. 5296-5306, Dec. 2018.

- [31] X. Li, G. Zhu, Y. Gong, and K. Huang, "Wirelessly powered data aggregation for IoT via over-the-air functional computation: Beamforming and power control," [Online]. Available: <https://arxiv.org/pdf/1808.04616.pdf>, 2018.
- [32] G. Zhu and K. Huang, "Mimo over-the-air computation for high-mobility multi-modal sensing," *IEEE Internet of Things Journal*, pp.1-1, 2019.
- [33] M. Goldenbaum and S. Stanczak, "Robust analog function computation via wireless multiple-access channels," *IEEE Transactions on Communication*, vol. 61, no. 9, pp. 3863-3877, September 2013.
- [34] C. H. Wang, A. S. Leong, and S. Dey, "Distortion outage minimization and diversity order analysis for coherent multiaccess," *IEEE Transactions Signal Processing*, vol. 59, no. 12, pp. 6144-6159, December 2011.
- [35] M. Goldenbaum and S. Stanczak, "On the channel estimation effort for analog computation over wireless multiple-access channels," *IEEE Wireless Communication Letters*, vol. 3, no. 3, pp. 261-264, June 2014.
- [36] X. Li, G. Zhu, Y. Gong, and K. Huang, "Wirelessly powered over-the-air computation for high-mobility sensing," *2018 IEEE Globecom Workshops (GC Wkshps)*, December 2018, pp. 1-6.
- [37] A. A. Khuwaja, Y. Chen, N. Zhao, M. Alouini, and P. Dobbins, "A survey of channel modeling for UAV communications," *IEEE Communications Surveys and Tutorials*, vol. 20, no. 4, pp. 2804-2821, Fourth Quarter 2018.
- [38] V. Liu, A. Parks, V. Talla, S. Gollakota, D. Wetherall, and J. R. Smith, "Ambient backscatter: Wireless communication out of thin air," in *Proc. of ACM SIGCOMM*, Hong Kong, China, Aug. 2013, pp. 39-50.
- [39] N. Zhang, J. Wang, G. Kang, and Y. Liu, "Uplink non-orthogonal multiple access in 5G systems," *IEEE Communications Letters*, vol. 20, no. 3, pp. 458-461, Mar. 2016.
- [40] Q. Wu, Y. Zeng, and R. Zhang, "Joint trajectory and communication design for multi-UAV enabled wireless networks," *IEEE Transactions on Wireless Communications*, vol. 17, no. 3, pp. 2109-2121, Mar. 2018.
- [41] Y. Liu, M. Derakhshani, and S. Lambotharan, "Outage analysis and power allocation in uplink non-orthogonal multiple access systems," *IEEE Communications Letters*, vol. 22, no. 2, pp. 336-339, Feb. 2018.
- [42] Z. Zhang, H. Sun, and R. Q. Hu, "Downlink and uplink non-orthogonal multiple access in a dense wireless network," *IEEE Journal on Selected Areas in Communications*, vol. 35, no. 12, pp. 2771-2784, Dec. 2017.

- 
- [43] S. S. Szyszkowicz and H. Yanikomeroglu, "Limit theorem on the sum of identically distributed equally and positively correlated joint lognormals," *IEEE Transactions on Communications*, vol. 57, no. 12, pp. 3538-3542, Dec. 2009.
- [44] S. Asmussen and L. Rojas-Nandayapa, "Asymptotics of sums of lognormal random variables with gaussian copula," *Statistics and Probability Letters*, vol. 78, no. 16, pp. 2709-2714, Nov. 2008.
- [45] N. A. Marlow, "A normal limit theorem for power sums of independent normal random variables," *Bell System Technical Journal*, vol. 46 (9), pp. 2081-2089, Nov. 1967.
- [46] Y. Zeng, R. Zhang and T. J. Lim, "Throughput Maximization for UAV-Enabled Mobile Relaying Systems," in *IEEE Transactions on Communications*, vol. 64, no. 12, pp. 4983-4996, Dec. 2016.
- [47] G. Zhu, S. Ko, and K. Huang, "Inference From Randomized Transmissions by Many Backscatter Sensors," in *IEEE Transactions on Wireless Communications*, vol. 17, no. 5, pp. 3111-3127, May 2018.
- [48] Vincent Liu, Aaron Parks, Vamsi Talla, Shyamnath Gollakota, David Wetherall, and Joshua R. Smith, "Ambient backscatter: wireless communication out of thin air," In Proceedings of the ACM SIGCOMM 2013 conference on SIGCOMM (SIGCOMM '13). ACM, New York, NY, USA, 39-50.
- [49] J. Wang, H. Hassanieh, D. Katabi, and P. Indyk, "Efficient and reliable low-power backscatter networks", SIGCOMM, 2012.
- [50] Z. Yang et al., "Joint Altitude, Beamwidth, Location, and Bandwidth Optimization for UAV-Enabled Communications", in *IEEE Communications Letters*, vol. 22, no. 8, pp. 1716-1719, Aug. 2018.